Medical Microbiology and Immunology (2019) 208:609–629
https://doi.org/10.1007/s00430-018-0564-z

ORIGINAL INVESTIGATION

Biogenic Au@ZnO core–shell nanocomposites kill *Staphylococcus aureus* without provoking nuclear damage and cytotoxicity in mouse fibroblasts cells under hyperglycemic condition with enhanced wound healing proficiency

Md. Imran Khan[1] · Susanta Kumar Behera[2] · Prajita Paul[1] · Bhaskar Das[3] · Mrutyunjay Suar[1] · R. Jayabalan[3] · Derek Fawcett[4] · Gerrard Eddy Jai Poinern[4] · Suraj K. Tripathy[1,5] · Amrita Mishra[1]

Received: 24 April 2018 / Accepted: 27 September 2018 / Published online: 5 October 2018

Abstract

The aim of the present study is focused on the synthesis of Au@ZnO core–shell nanocomposites, where zinc oxide is overlaid on biogenic gold nanoparticles obtained from *Hibiscus Sabdariffa* plant extract. Optical property of nanocomposites is investigated using UV–visible spectroscopy and crystal structure has been determined using X-ray crystallography (XRD) technique. The presence of functional groups on the surface of Au@ZnO core–shell nanocomposites has been observed by Fourier transforms infrared (FTIR) spectroscopy. Electron microscopy studies revealed the morphology of the above core–shell nanocomposites. The synthesized nanocomposite material has shown antimicrobial and anti-biofilm activity against *Staphylococcus aureus* and Methicillin Resistant *Staphylococcus haemolyticus* (MRSH). The microbes are notorious cross contaminant and are known to cause infection in open wounds. The possible antimicrobial mechanism of as synthesized nanomaterials has been investigated against *Staphylococcus aureus* and obtained data suggests that the antimicrobial activity could be due to release of reactive oxygen species (ROS). Present study has revealed that surface varnishing of biosynthesized gold nanoparticles through zinc oxide has improved its antibacterial proficiency against *Staphylococcus aureus*, whereas reducing its toxic effect towards mouse fibroblast cells under normal and hyperglycaemic condition. Further studies have been performed in mice model to understand the wound healing efficiency of Au@ZnO nanocomposites. The results obtained suggest the possible and effective use of as synthesized core shell nanocomposites in wound healing.

Keywords Biofilm · Core–shell · Gold · *Staphylococcus aureus* · Methicillin resistant *Staphylococcus haemolyticus* · Zinc oxide

Introduction

Raise in bacterial infections and decrease in the antibiotic susceptibility are considered as two major issues which can adversely affect the public health globally, particularly those living in developing countries [1, 2]. Among various pathogens, *Staphylococcus aureus* (*S. aureus*) is potential

Electronic supplementary material The online version of this article (https://doi.org/10.1007/s00430-018-0564-z) contains supplementary material, which is available to authorized users.

✉ Amrita Mishra
amrita.mishra@kiitbiotech.ac.in

[1] School of Biotechnology, Kalinga Institute of Industrial Technology (KIIT), Bhubaneswar, Odisha 751024, India

[2] IMGENEX India Pvt. Ltd., Bhubaneswar, India

[3] Department of Life Sciences, National Institute of Technology, Rourkela, Odisha 769008, India

[4] Murdoch Applied Nanotechnology Research Group, Department of Physics, Energy Studies and Nanotechnology, School of Engineering and Energy, Murdoch University, Murdoch, WA, Australia

[5] School of Chemical Technology, Kalinga Institute of Industrial Technology (KIIT), Bhubaneswar 751024, Odisha, India

source of bacteremia, which is known to be associated with higher morbidity and mortality [3, 4]. The problem of *S. aureus* bacteremia (SAB) is not only high in terms of cost and utilization but also it can enhance the threat of infectious endocarditis. Early diagnosis and appropriate treatment is essential since SAB infection may cause proliferation of other metastatic foci thereby increasing the risk of mortality [5, 6]. In recent years, clinical complications associated with SAB has increased rapidly due to the increase in the frequency of invasive procedures, numbers of immunocompromised patients, and resistance of *S. aureus* strains to available antibiotics [7]. In addition, if the patient diagnosed with SAB is known to have a previous history of yperglycemia, then it becomes a tortuous situation for the practicing physician. A recent study undertaken by Kanafani et al. has suggested that the complications from SAB are higher in diabetic patients with significant mortality rate (22.1%) [8]. Moreover, biofilms formed by this particular bacterium has been recognized as the most frequent cause of biofilm-associated infections. Host immune responses and effect of antibiotics against persistent biofilm infections are generally considered to be less effective and hence may lead to chronic diseases [9]. Since the dispersal of cells from biofilm can facilitate spread of infection to various secondary sites, it can intensify clinical complications particularly in case of patients with hyperglycemia [10]. This change in epidemiology along with the ingrained virulence of the pathogen and the ability to form biofilm, demands the development of improved antibiotic agents to prevent and treat SAB associated complications. In this respect, nano-therapeutic agents have established abundant attraction in the scientific community due to their distinctive antimicrobial activity which might be due to the synergistic effect of small size and high surface-to-volume ratio that permits close interfaces near microbial membranes. This particular aspect is also expected to be effective against bacterial biofilms. In the recent past, ZnO nanoparticles (ZnO NPs) have displayed promising results towards *S. aureus* [11, 12]. However, the probable toxicity against healthy cells and tissues has impeded their further development and possible clinical trials [13, 14]. To overcome such practical complications, fabrication of metal/ZnO nanocomposites (NCs) has been proposed, which may preserve the antimicrobial action of the ZnO NPs and improve the biocompatibility of the resultant material. One of the fundamental reasons behind designing NCs is focused on increasing the antibacterial activities of the as synthesized NCs by influencing their natural composition, structural behavior and morphologies, however, posing minimum damage towards healthy cells and tissues. Recently our group has demonstrated the antifungal activity of Ag@ZnO core–shell NCs against *Candida krusei* [15]. However, to the best of our knowledge, such structures have never been explored for antibacterial and anti-biofilm application against SAB.

Keeping this in view; in the current report we have synthesized Au@ZnO core–shell NCs, where thin layer of ZnO is coated on Au NPs. Au NPs are known to be more biocompatible than other inorganic nanomaterials and hence it is expected that the resultant hetero-nano-junction will have improved biocompatibility. Au NPs have been synthesized using *Hibiscus sabdariffa* (HS) plant leaf extract and coating of ZnO is done by the addition of zinc nitrate hexahydrate in alkaline condition. As the NCs is synthesized using the extract of HS, it may add various properties which are medically relevant to the overall system. Polyphenolic compounds present in the extract of this plant is known to inhibit hyperglycemia, hyperlipidemia, and glycation-oxidative stress whereas improving insulin resistance [16]. Keeping this in view, the antibacterial and anti-biofilm activity of Au@ZnO NCs have been investigated against *S. aureus* and MRSH. Further detailed study has been conducted to understand the possible antimicrobial mechanism of as synthesized NCs against *S. aureus*. In vitro experiments such as intracellular measurement of ROS and DNA degradation have been performed. The cytotoxicity and genotoxicity of Au@ZnO NCs, ZnONPs and Au NPs have been tested against mouse fibroblast cells under normal and hyperglycemic conditions. In vitro antibacterial activity has also been checked in *S. aureus* infected cell line and we have got promising results with as synthesized Au@ZnO NCs. Further, the wound healing potential of the resultant NC system has been evaluated on mouse model and results suggest that NCs may have potential applications in would healing and biofilm control.

Materials and methods

Materials

Gold (III) chloride trihydrate ($HAuCl_4.3H_2O$, 99.0%), zinc nitrate hexahydrate ($ZnNO_3.6H_2O$, 99.0%), crystal violet and all the microbial and animal cell culture medium were obtained from Himedia (Mumbai). All antibodies, sodium hydroxide (NaOH), sodium chloride (NaCl), acetic acid (glacial) 100%, methanol, agarose, 2′,7′-dichlorofluorescin diacetate (DCF-DA), Fluoresein diacetate (FDA) and propidium iodide (PI) were purchased from Merck (Germany). All the materials were used as received without further purification.

Extraction of plant leaf extract and Au NPs synthesis

Hibiscus sabdariffa were purchased from local market. 20 g of leaf were washed thrice using distilled water and crushed with 40 mL of de-ionized (DI) water by mortar pestle and filtered using vacuum filter (Whatman No. 1). Then filtrate

was taken for the biosynthesis of Au NPs. Au NPs were synthesized according to earlier reported protocol [17].

Synthesis of Au@ZnO core–shell NCs

Encapsulation of the Au NPs with ZnO was achieved by following previously reported protocol [15]. 2 mL of NaOH (2M) was taken and added into 10 mL of 10 mM zinc nitrate hexahydrate to get white precipitate of zinc hydroxide. Formed precipitate was dissolved with addition of excess amount of NaOH (2M) solution to get sodium zincate. Sodium zincate (5 mL) was added to 50 mL of biosynthesized Au NPs in stirring condition 90 ± 2 °C. To synthesize Au@ZnO NCs, reaction was stirred for 30 min and color changing from reddish-purple to blackish-purple indicated the development of Au@ZnO core–shell NCs. The final concentration of zinc nitrate hexahydrate was ~ 1 mM.

Optimization of reaction parameters for Au@ZnO NCs synthesis

Three parameters which were considered to be critical for the synthesis of NCs i.e. concentration of zinc nitrate hexahydrate, reaction temperature and pH were optimized for obtaining the most favourable reaction condition. All the parameters were optimized at a reaction volume of 50 mL. The process was first optimised for the concentration of zinc nitrate hexahydrate and temperature. Four different concentrations (0.5 mM, 1 mM, 1.5 mM and 2 mM) of zinc nitrate hexahydrate were used for the synthesis of ZnO shell on Au NPs at 90 °C. The data obtained from UV–Vis spectrophotometer suggested that ~ 1 mM of zinc nitrate hexahydrate was optimum, and thus showed good result. Following this, with ~ 1 mM zinc nitrate hexahydrate, four altered temperatures (room temperature i.e. 25 ± 2 °C, 50 °C, 70 °C and 90 °C) were selected for the synthesis and the reaction was found to produce desired results at 90 °C. These two parameters were further used to optimize the pH (natural pH 3.34, 4.0, 6.0, 8.0 and 10.0) of reaction system. UV–Vis spectrophotometer results indicated that the optimum pH for the system was 3.34 (natural).

Structural and morphological characterization of the materials

To monitor the formation of Au NPs and Au@ZnO NCs, UV–Vis spectroscopy (Cary 100 UV–Vis, Agilent technologies) was performed. The NPs and NCs synthesized under optimized condition were characterized using different instrumental techniques. Morphology of the materials was analyzed using High-resolution transmission electron microscopy (TEM, JEOL-JEM-2010). Further, X-ray diffraction technique (XRD, D/Max 2005, Rigaku) was used to investigate the crystal structure of the materials. Surface functional groups of as synthesized nanomaterials was observed through Fourier transform infrared spectrophotometer (FTIR, Shimadzu 8201PC, Japan).

Investigation of stability of Au@ZnO NCs under hyperglycemic condition

To investigate the stability of as synthesized Au@ZnO NCs under hyperglycemic conditions, optimum concentration of the NC (100 µg/mL) was challenged with different concentrations (0, 10, 20, 30, 40 and 50 mM) of glucose at room temperature (25 ± 2 °C) and at 37 °C for 7 days. UV–Visible spectrophotometer was used to analyze the results.

Colony forming unit (CFU) assay

The antibacterial activity of the synthesized nanomaterials was observed against two Staphylococcal strains. Methicillin resistant *Staphylococcus haemolyticus* (MRSH) isolated from environment and *S. aureus* (MTCC-3160) purchased from Microbial Type Culture Collection and Gene Bank (MTCC), Chandigarh were taken for this study. Both the bacterial cultures were maintained in nutrient media at 37 °C. Antibacterial action of Au NPs, ZnO NPs and Au@ZnO NCs was investigated against MRSH and *S. aureus* through CFU assay. Single colony of bacteria was picked from nutrient agar (NA) plate and inoculated into 10 mL of nutrient broth (NB) test tube. The later was incubated in a refrigerated shaking incubator (Shaking Incubator, LabTech, Daihan Labtech) at 37 °C for 12 h. 100 µL of grown culture from the above tube was taken and further inoculated into fresh 100 mL NB and incubated at 37 °C for 6 h (stationary phase) in a refrigerated shaking incubator. After incubation, 1 mL of bacterial cells were collected in 1.5 mL microcentrifuge tube (MCT) followed by centrifugation at 8000 rpm (5 min) and washed with 1X PBS buffer. The pellet was re-suspended into fresh 1 mL NB, which was later used for inactivation experiment. CFU assay was done by inoculating 1×10^6 CFU/mL of bacterial cells into a final volume of 20 mL NB with varied concentrations (0, 50, 100, 250, 500 and 750 µg/mL) of nanomaterials and incubated at 37 °C for 12 h in shaking incubator (200 rpm). At 3 h interval, 100 µL of sample was withdrawn and serially diluted (10^{-1} to 10^{-5}) using 0.9% NaCl (normal saline solution) and 10^{-5} dilution was used for plating on NA by spread plate technique to conclude the bacterial cell growth inhibition by CFU assay.

Crystal violet assay

To examine the comparative anti-biofilm efficacy of Au NPs, ZnO NPs and Au@ZnO NCs against MRSH and *S. aureus*, crystal violet assay was performed [18]. Biofilm formation

was initiated by seeding 1 mL of bacterial culture in NB (~ 10^7 CFU/mL) into 24-well polystyrene microtitre plates (Nest Biotechnology Co., Ltd., USA) and incubated at 37 °C for 24 h in a static incubator to permit biofilm development. Subsequently, non-adhered cells were removed followed by washing the wells three times using 1 mL of 1X PBS. Thereafter, the existing biofilm was incubated for 24 h in NB which were supplemented with various concentration (0, 50, 100, 250, 500 and 750 µg/mL) of nanomaterials. After treatment, nanomaterials containing culture media were discarded and wells were washed using 1 mL of 1X PBS. Biofilm was fixed using absolute methanol for 15 min and dried for 1 h at 37 °C. Treated and untreated biofilms were stained with crystal violet (0.1% in DH_2O) and incubated for 45 min at 37 °C. Biofilms incubated with NB only were used as control. After incubation, stains were removed and washed using 1X PBS. To solubilize the crystal violet stains, 1 mL of acetic acid (33% v/v) was added into each well and absorbance was taken at 590 nm using UV–visible spectrophotometer. Acetic acid (33% v/v) was used as blank. % of biomass was calculated according to the following Eq. (1):

$$\%\ \text{of Biomass} = \frac{\text{Abs}_{590\text{nm}}\ \text{Treated} - \text{Abs}_{590\text{nm}}\ \text{Blank}}{\text{Abs}_{590\text{nm}}\ \text{Control}} \times 100 \quad (1)$$

Evaluation of bacterial cells viability through fluorescence microscopy

Live/dead staining was conducted to investigate the viability of *S. aureus* after treating with as synthesized nanomaterials. Assay was done according to manufacturer protocol (LIVE/DEAD™ BacLight™ Bacterial Viability Kit, Invitrogen™). Briefly, *S. aureus* cells were treated with 100 µg/mL of Au NPs, ZnO NPs and Au@ZnO NCs for 0, 6 and 12 h. Culture media were discarded followed by centrifugation and obtained pellet was washed using 1× PBS. The pellets were re-suspended in 1X PBS. SYTO9 and propidium iodide was added into treated and untreated samples followed by its incubation at room temperature (RT) for 15 min under dark condition. Results were analyzed under fluorescence microscope (Life Technologies, USA) at 40× magnification of objective.

Determination of reactive oxygen species (ROS)

Intracellular reactive oxygen species (ROS) was qualitatively measured using DCF-DA under fluorescence microscopy [19]. DCF-DA is a particular dye which enter into the cells inertly and counters with ROS to form greatly fluorescent dichlorofluorescein (DCF). In the present work, 1 mL *S. aureus* sample treated with Au NPs, ZnO NPs and Au@ZnO NCs (100 µg/mL) were selected, centrifuged and washed with 1X PBS. Further, cells were re-suspended in 1X PBS buffer with the addition of 10 µM of DCF-DA and incubated under dark condition for 15 min at 37 °C. Pictures obtained were analyzed through fluorescence microscope (Life Technologies, USA).

DNA degradation

Antimicrobial mechanism of nanomaterials against *S. aureus* was evaluated through DNA degradation assay. Microbial cells were incubated with 100 µg/mL of Au NPs, ZnO NPs and Au@ZnO NCs for 12 h. Isolation of DNA was performed followed by formerly reported protocol [20]. Obtained pellets of DNA were dissolved in nuclease free water (Himedia, Mumbai) and 5 µL of DNA sample from each tube was loaded on 1% agarose gel made in Tris acetate ethylene diamine tetra acetate (TAE) buffer and stained by ethidium bromide (1 µg/mL). Images were analyzed using gel documentation system (BioRad, USA).

Field Emission-Scanning Electron Microscope (FE-SEM)

Samples of treated and untreated *S. aureus* cells for FE-SEM analysis were prepared followed by previous protocol [21]. 1×10^6 CFU/mL of *S. aureus* was treated with 100 µg/mL of Au@ZnO NCs for 6 and 12 h. FE-SEM analysis was done following sputter coating of gold on treated and untreated samples.

Methylthiazole tetrazolium (MTT) assay

Cytotoxicity of Au NPs, ZnO NPs and Au@ZnO NCs has been investigated against mouse dermal fibroblast (isolated from BALB/c mouse at IMGENEX India Pvt. Ltd., Bhubaneswar, India) and macrophage (RAW 267.4) cell line through standard MTT assay and the formazan produced is quantified using Microplate reader (Bio-Rad, USA, model 680) [22]. Cells were maintained in Dulbecco's Modified Eagle's Medium (DMEM), supplemented with 10% Fetal Bovine Serum (FBS). Initially, 5×10^4 cells in DMEM (10% FBS) were plated into 24 well plate and incubated in the presence of 5% CO_2 in a humidified incubator at 37 °C for 24 h to confluence the cells to 70–80%. For control, three wells were taken with medium alone and this was considered as blank for absorbance readings. Following incubation, media was taken out from the wells with the help of aspirator and nanomaterials (50, 100 and 250 µg/mL of Au NPs, ZnO NPs and Au@ZnO NCs) supplemented growth medium was added into the wells. Hyperglycemic conditions were made with the addition of 50 mM of D-glucose (D-glu). To maintain osmoregularity, 50 mM of L-glucose (L-glu) was also added. The cells were incubated in the presence of 5% CO_2 in a humidified incubator at 37 °C for 24 h.

After that, supernatant was aspirated out and the cells were washed with 1× PBS buffer. MTT reagent (0.5 mg/mL) was added into respective wells. The wells were incubated for 2 to 4 h to form purple precipitate. Results were analysed by taking absorbance at 570 nm using Microplate reader. Percentage (%) viability of cells was deliberated using following formulae:

$$\% \text{ Viability} = \frac{[(\text{Abs of treated} - \text{Abs of blank})]}{[(\text{Abs of untreated} - \text{Abs of blank})]} \times 100 \quad (2)$$

Viability assessment of fibroblast through live/dead assay

FDA and PI stains is used to investigate the viability of fibroblast cells after treatment with nanomaterials. FDA stains live cells giving green color whereas dead cells turn into red color by PI. Staining was performed followed by previously reported protocol with some modifications [23]. Culture condition, concentration and confluency of cells was same as mentioned in MTT assay. Cells were treated with 100 µg/mL of nanomaterials (Au NPs, ZnO NPs and Au@ZnO NCs) for 24 h. After treatment, medium was removed and washed with 1X PBS. To stain the cells, 500 µL of 1× PBS was added into each well. Subsequently 20 µg/mL of FDA and 50 µg/mL of PI was added and kept under dark for 15 min at RT. After incubation, staining solution was aspirated and washed with 1× PBS to remove excess amount of stains. Images were analyzed under inverted fluorescent microscope at 40× objective lens (Life Technologies, USA).

DAPI (4′,6-Diamidino-2-Phenylindole, Dihydrochloride) assay

Genotoxicity of Au NPs, ZnO NPs and Au@ZnO NCs against fibroblast cells was also investigated. Briefly, cells were treated with 100 µg/mL of nanomaterials for 24 h and washed with 1× PBS buffer followed by addition of 10 µg/mL DAPI stain and incubated under dark for 10 min at room temperature. Changes in the nuclear morphology was examined using fluorescence microscope at 40× magnification of objective lens (Life Technologies, USA).

Western blotting

Fibroblast cells were grown and incubated with 100 µg/mL of Au NPs, ZnO NPs and Au@ZnO NCs for 24 h under normal and hyperglycemic conditions. After treatment, nanomaterials containing media were removed and washed with 1X PBS buffer. Untreated and treated cells were lysed using Radioimmunoprecipitation assay buffer (RIPA buffer) in the presence of protease and phosphate inhibitor. Protein concentration was estimated through Bradford assay. Extracted proteins were resolved on 10% sodium dodecyl sulfate polyacrylamide gel electrophoresis (SDS–PAGE), electrotransferred to polyvinylidene difluoride (PVDF) membrane and probed with primary antibody: β-actin, GAPDH and ERK1/2. After incubation with secondary antibody which was conjugated with horseradish peroxidase, the immune complexes were pictured using enhanced chemiluminescent (ECL) substrate for horseradish peroxidase (HRP) according to the manufacturer's protocol (Thermo Fisher Scientific, USA).

Enzyme-Linked Immunosorbent Assay (ELISA) to measure the level of cytokines

Protein extract were collected from fibroblast cells which was treated with Au NPs, ZnO NPs and Au@ZnO NCs (100 µg/mL) under normal and hyperglycemic conditions. The level of cytokines: IL 6 and IL 22 was measured using ELISA kit (Thermo Fisher Scientific, USA).

Intracellular antimicrobial activity of nanomaterials against *S. aureus*

For this experiment, optimum concentration (100 µg/mL) of nanomaterials were selected. Mouse dermal fibroblast (5×10^4) cells were seeded in 24 wells plate and incubated for 24 h at 37 °C in humidified incubator in the presence of 5% CO_2. Subsequently cells (80% confluent) were exposed to *S. aureus* (~ 1×10^6) at multiplicity of infection (MOI) 10 for 1 h and 20 µg/mL gentamicin were added and incubated for 30 min to kill extracellular bacteria. Infected cells were treated with 100 µg/mL of Au NPs, ZnO NPs and Au@ZnO NCs under normal and hyperglycemic condition for 12 and 24 h. *S. aureus* infected dermal fibroblast cells (untreated) were used as control. After incubation, extracellular media was aspirated and cells were lysed using 0.1% Triton-X100. To check intracellular survival of *S. aureus*, plating was done on NA plates by serial dilution of the samples and colonies were counted after 24 h of incubation at 37 °C in static incubator.

Wound creation and wound closure analysis

In this investigation, five to seven week old female BALB/c mice were used and preserved in cages in the compartment of high efficiency particulate air (HEPA)-filter in 12 h light cycles. Sterilized food (chow) and water *ad libitum* were given to each mice. All the experimentations were implemented according to national guidelines of animal care and were permitted by the Institutional Animal Ethical Committee.

A 6 mm-diameter full-thickness excisional wound was made on the dorsum of mice and separated in two categories.

Mice treated with 1× PBS were considered as the control specimens whereas mice treated with 100 µg/mL of Au@ZnO NCs suspended in 1× PBS were taken as experimental specimens. After 1 day of wound creation, 100 µg/mL of Au@ZnO suspended in 1× PBS were injected below the created wound or crust and treated for 1, 5, 10 and 15 days. Digital photography was performed to check morphological assessment, wound re-epithelialization and closure till the wound was totally healed. Photographs of wound were taken on day 0, 1, 5, 10 and 15 days after creating wound in control and treated mice. % of wound closure were calculated through following equation:

$$\% \text{ of wound closure} = \frac{D_0 - D_n}{D_0} \times 100 \quad (3)$$

In this equation, D_0 is the wound area at the day of wound created and D_n is the wound area at day "n".

Histological examination

Treated and untreated mice were sacrificed after 5 and 15 days of wound creation. The wound biopsies were excised, fixed with paraformaldehyde and embedded with paraffin. Following this, 4 µm thick central wound was processed, stained by hematoxylin and eosin to notice the migration and re-epithelialisation of fibroblasts as well as keratinocytes into the epidermal layer.

Statistical assessment

Statistical study was done via one-way analysis of variance (ANOVA) through Dunnett test (compared all columns vs control column) by PRISM software (GraphPad, San Diego, CA, USA). Data were expressed as the ± standard error of the mean (SEM). Variances were shown to be statistically significant for $p < 0.05$. Significant level of statistical analysis has been specified in the legend of images.

Results and discussion

Effect of process parameters on the formation of Au@ZnO NCs

Due to the abundance of free electrons on their surface, noble metal nanoparticles exhibit strong and stable Surface Plasmon Resonance (SPR) band in the UV–Visible spectrum. Coating by a metal oxide shell will encourage a modification in the dielectric constant of the neighboring environment and can induce an alteration in the SP band of the aqueous dispersion of metal NPs. This phenomenon has been employed to investigate the precipitation of zinc oxide shell on Au NPs. UV–Vis spectroscopy has been used to monitor the formation of Au NPs and Au@ZnO NCs. The resultant spectra are shown in Fig. 1a. This figure also includes the spectra of plant extract and gold salt solution (1 mM). Aqueous dispersion of biosynthesized Au NPs has shown strong SPR band at 535 nm, which indicates the formation of crystallites of 20 to 50 nm [24, 25]. Plant extract and aqueous solution of gold salt did not show any significant absorption peak. After the addition of aqueous sodium zincate solution, SPR band has red-shifted to 536 nm with a minor but distinct peak at 351 nm for ZnO NPs [26]. This minor shift could be due to the formation of ZnO shell which may have changed the dielectric constant around Au NPs ($n_{H2O} = 1.33$ and $n_{ZnO} = 1.92$). This optical occurrence could be attributed to the relocation of electronic charge among the metallic core and semiconductor shell. Due to the existence of surface charge, unprotected Au NPs will have a tendency to agglomerate and form larger crystal which in turn will diminish their nano-size dependent antibacterial properties. Owing to the large change between the intrinsic Fermi level of the Au and conduction band of ZnO (n-type semiconductor), mobile electrons which diffuse inside the shell will be confined for extended periods of time in the central core. It can reduce the intimate interface between the nearby NPs and, therefore, may increase the stability of the resultant NC structure. In addition to the major peak at 537 nm, a shoulder peak is also noticed at 351 nm. It is proposed that, formation of ZnO shell may have taken some time (usually 30 min). Prior to the encapsulation process, few Au NPs might have agglomerated and made massive clusters. This may have produced dipole pairing amid closely relating metal particles which could have induced a large alteration in the environment around metal particles [27, 28].

This hypothesis has been supported by the electron microscopy images. However, after the formation of ZnO shell, agglomeration of metal NPs is restricted. Aqueous zinc nitrate further dissociates to yield Zn^{2+} and NO_3^- ions. In the appearance of sodium hydroxide, Zn^{2+} may possibly precipitate to develop $Zn(OH)_2$. The resulting $Zn(OH)_2$ is expected to produce $[Zn(OH)_3 \cdot H_2O]^-$ in presence of excess amount of NaOH and water. Instantly under hydrothermal state, solvated zincate ion can convert to make $[Zn(OH)_4]^{2-}$. However, these $[Zn(OH)_4]^{2-}$ ions may nucleate on the surface of Au NPs followed by thermal decomposition to form ZnO and H_2O, which may also convert to $Zn(OH)_2$ and further decompose to make ZnO [29]. In this regard, optimization of reaction parameters is crucial not only to get maximum yield of the preferred production but also to scale-up the biosynthesis protocols. Effect of three process parameters viz. concentration of sodium zincate solution, reaction temperature and pH has been investigated. With increase in the concentration of the sodium zincate solution from 0.5 to 1.0 mM, intensity of both the peaks corresponding to

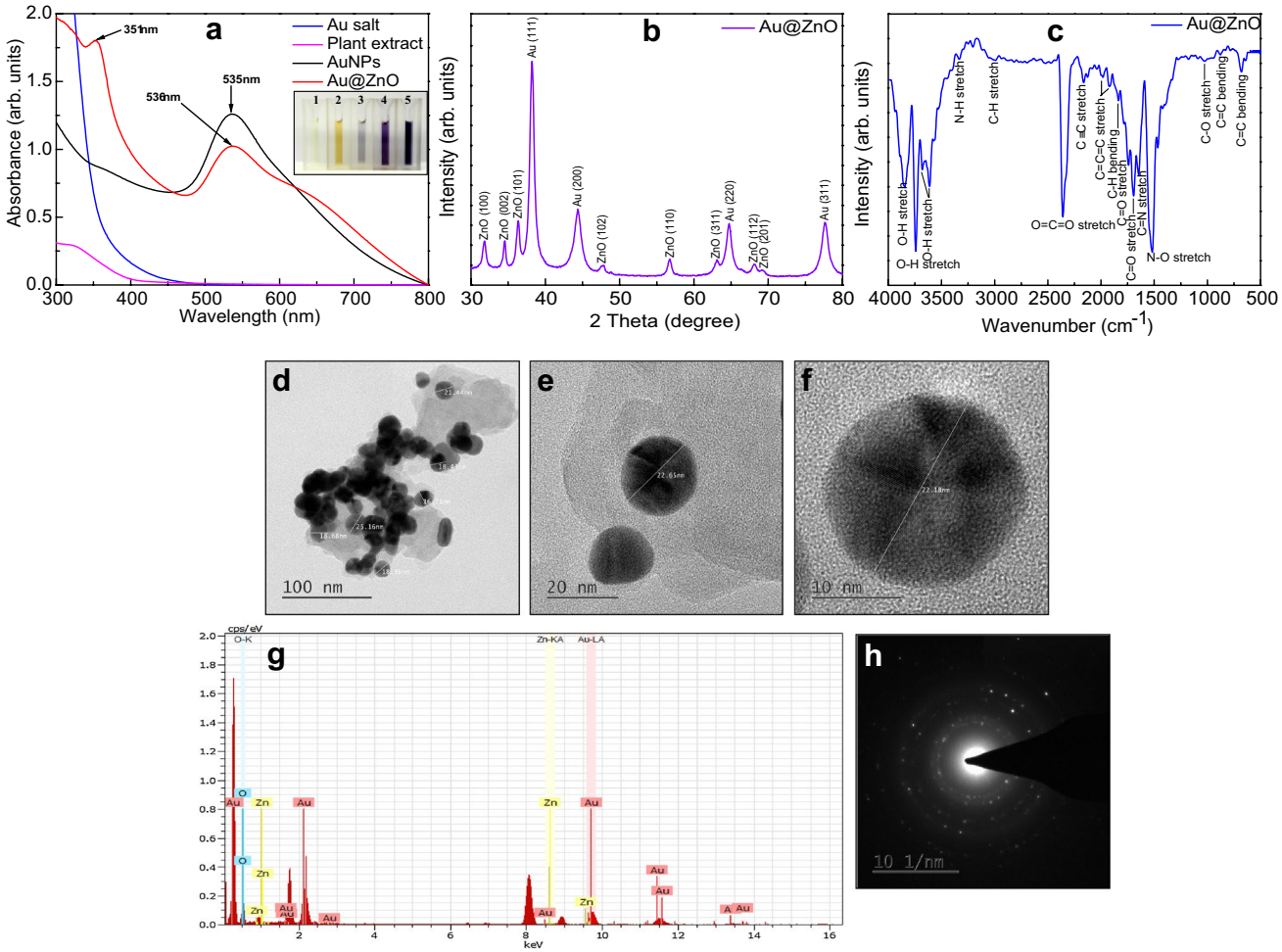

Fig. 1 Au NPs and Au@ZnO NCs were synthesized using *Hibiscus Sabdariffa* leaf extracts and characterized through **a** UV–Visible spectrophotometer, **b** X-ray diffraction and **c** FTIR. Electron microscopy images of Au@ZnO core–shell NCs: **d** TEM, **e, f** HR-TEM, **g** EDAX and **h** SAED. Image in the index of **a**, indicates the color changes in the solution. (1) Au salt, (2) plant extracts, (3) Au salt + plant extract, (4) Au NPs and (5) Au@ZnO NCs

Au@ZnO NCs has increased (Figure S1a). Similarly, beyond 1.0 mM, any further increase in the concentration of the zincate solution has resulted in sharp damping of both the peaks in the absorption spectrum. With 1.0 mM of sodium zincate solution, maximum intensity of both the peaks corresponding to Au@ZnO NCs has been obtained. It is expected that lower concentration would not have produced enough ZnO colloid for complete encapsulation of Au NPs. Similarly, at a higher concentration, large amount of free $[Zn(OH)_4]^{2-}$ ions might have been produced which could have resulted in damping of the SPR band corresponding to Au@ZnO NCs. However, when the temperature of the reaction system is maintained at 25 or 50 °C, SPR band did not shift remarkably. Minor shift in SPR band has been noticed with increase in reaction temperature to 70 °C. This is further enhanced by increasing the temperature to 90 °C with the formation of two distinct peaks (536 and 351 nm) (Figure S1b). In addition, at low reaction temperature (e.g. 25 °C), free $[Zn(OH)_4]^{2-}$ ions will not be transferred to ZnO and hence will not be able to form Au@ZnO NCs. Thus, any shift in the SPR band is not noticed. With increase in the reaction temperature (beyond 70 °C), the formation of nanocrystalline ZnO is facilitated and hence shift of the SPR band is observed.

Characterization of Au@ZnO core–shell NCs

Crystal phase and structure of Au@ZnO NCs has been investigated by XRD and results are presented in Fig. 1b. Obtained data has shown twelve diverse peaks for as synthesized NCs. Three peaks at $2\theta = 38.21$, 44.35, 64.75 and 77.6 were assigned to (111), (200), (220) and (311) planes of face centered cubic structure of metallic gold (JCPDS 04-0784) with Fm3m planetary group symmetry. Similarly, peaks at $2\theta = 31.8$, 34.55, 36.35, 47.9, 56.8, 63.1, 68.1, and 69.15 corresponds to (100), (002), (101), (102), (110), (311),

(112), and (201) wurtzite phase of ZnO planes (JCPDS 36-1451). Scherrer's equation is used to calculate the mean crystallite diameter (MCD) of as synthesized nanomaterials, and the size is found to be ≈22 nm and 31 nm for Au NPs and Au@ZnO NCs respectively. In the XRD pattern of the NCs, any peak which might attribute to the gold oxides (i.e. Au_2O, Au_2O_3 etc.) or Zn–Au–O compounds has not been observed.

The occurrence of adsorbed particles and functional groups on the surface can have significant role on the antimicrobial activity of the nanomaterials. Thus, functional group present on the surface of Au@ZnO NCs have been investigated using FTIR spectroscopy in the range of 500–4000 cm^{-1} to understand its surface chemistry. The FTIR spectrum of as-synthesized Au@ZnO NCs is shown in Fig. 1c. Sharp band at 3844, 3742, 3681, 3611 cm^{-1} may relate to O–H stretch of vibration. At 3334 and 2989 cm^{-1}, small vibration is observed, which may be due to the stretching peak of N–H and C–H group, respectively. The strong embarking stretch of side chain for O=C=O group is obtained at 2359 cm^{-1}. The weak and small band is shown at 2163 cm^{-1} which may correspond to C≡C group. Two small vibrational stretch of C=C=C is observed at 1982 and 1919 cm^{-1} which comes between 2000 and 1900 cm^{-1}. A weak bending at 1835 cm^{-1} is seen which may resemble to the vibration of C–H group. Two small and distinct stretch is seen at 1741 and 1692 cm^{-1}, which may relay for the C=O. A small and medium stretch at 1645 cm^{-1} is detected for C=N. A strong and sharp stretch band at 1517 cm^{-1} is noticed, which may correspond to N–O stretch. Small vibrational stretch of C–O is seen at 1025 cm^{-1} which originate between 1075–1020 cm^{-1}. A small vibration at 878 cm^{-1} and a sharp and distinct band at 681 cm^{-1} are observed, which suggests the bending of C=C [30].

Morphology of the Au@ZnO NCs is studied using TEM and resultant pictures are revealed in Fig. 1. Samples for TEM analysis, have been processed by dipping the TEM grid in aqueous dispersion of nanomaterials followed by freeze drying for 12 h. Formation of core–shell morphology with near-spherical Au NPs with a size range of 16 to 25 nm capped within ZnO shell are clearly observed (Fig. 1d, e). Thickness of the oxide shell is found to be 15 to 20 nm. In the present case, multiple Au NPs is found to be encapsulated within single ZnO shell. Comparable results have been previously obtained by other researchers [31]. As shown in Fig. 1f, the core has an inter planar positioning of 0.236 nm, which matches to the (111) plane face centered cubic (FCC) structure of metallic gold [32]. The distance among adjacent lattice fringes at the gold-zinc oxide hetero-junction is 0.29 nm, which is near to the d-spacing of the (100) plane of hexagonal ZnO (exact value is 0.287 nm). Chemical composition of Au@ZnO NCs is investigated by TEM Energy Dispersive X-ray Spectrometry (EDS) technique. As shown in Fig. 1g, NCs have shown clear peaks corresponding to Au, Zn, and O. TEM SAED pattern rings are shown in Fig. 1h. Size distribution and surface charge of Au@ZnO NCs is inspected by differential light scattering (DLS) and zeta potential technique, respectively. As displayed in Figure S2a and b, average range of size for NCs is 134.3 nm and obtained surface charge is − 19.7 mV.

Stability of Au@ZnO NCs under hyperglycemic condition

Stability is the foremost challenge in practical application of nanostructures in real working environment [33]. According to the American Association of Diabetes, a hyperglycemic situation is usually doubted if the random plasma glucose in patient sample accounts to ≥200 mg/dl or 11.1 mmol/L. Thus stability of the as synthesized and purified NCs is investigated by keeping the dispersion undisturbed at 37 °C in increasing concentrations of glucose. As shown in Figure S3 and S4, the SPR band of the aqueous distribution of Au@ZnO NCs is not altered remarkably. This suggests that any significant structural modification in the particle size of NCs is not registered inspite of an incubated time duration of 7 days' treatment with glucose.

Antimicrobial efficiency of nanomaterials

Antibacterial action of Au NPs, ZnO NPs and Au@ZnO NCs has been investigated against MRSH and *S. aureus* through CFU assay. As observed from Fig. 2, the effectiveness of ZnO NPs as compared to biosynthesized Au NPs is very high since lower concentration of the metal oxide NPs has inhibited the growth of both MRSH and *S. aureus*. Data shown in Fig. 2a clearly suggests that lesser concentrations of Au NPs (50 and 100 µg/mL) has not shown any antibacterial activity against both pathogens. After 12 h incubation, percentage of *S. aureus* viability is observed to be approximately 50.83, 44.55 and 24.67% with 250, 500 and 750 µg/mL of Au NPs respectively. Against MRSH the antibacterial effect is observed with only 500 and 750 µg/mL of Au NPs after 12 h incubation (Fig. 2d). In contrast, when bacterial cells are treated with chemically synthesized ZnO NPs, the antibacterial activity has been observed with the lowest concentration of ZnO (50 µg/mL) following 12 h of incubation against *S. aureus* and MRSH (Fig. 2b, e). 100, 250 and 500 µg/mL concentration of ZnO NPs inhibited *S. aureus* growth completely within 9, 6 and 3 h of incubation, respectively, whereas 750 µg/mL of ZnO NPs killed the bacteria within 3 h of incubation. Data shown in Fig. 2e suggests that the antibacterial activity of ZnO NPs against MRSH is higher than *S. aureus* at 250, 500 and 750 µg/mL concentration. Moreover, the time taken to suppress the growth of *S. aureus*

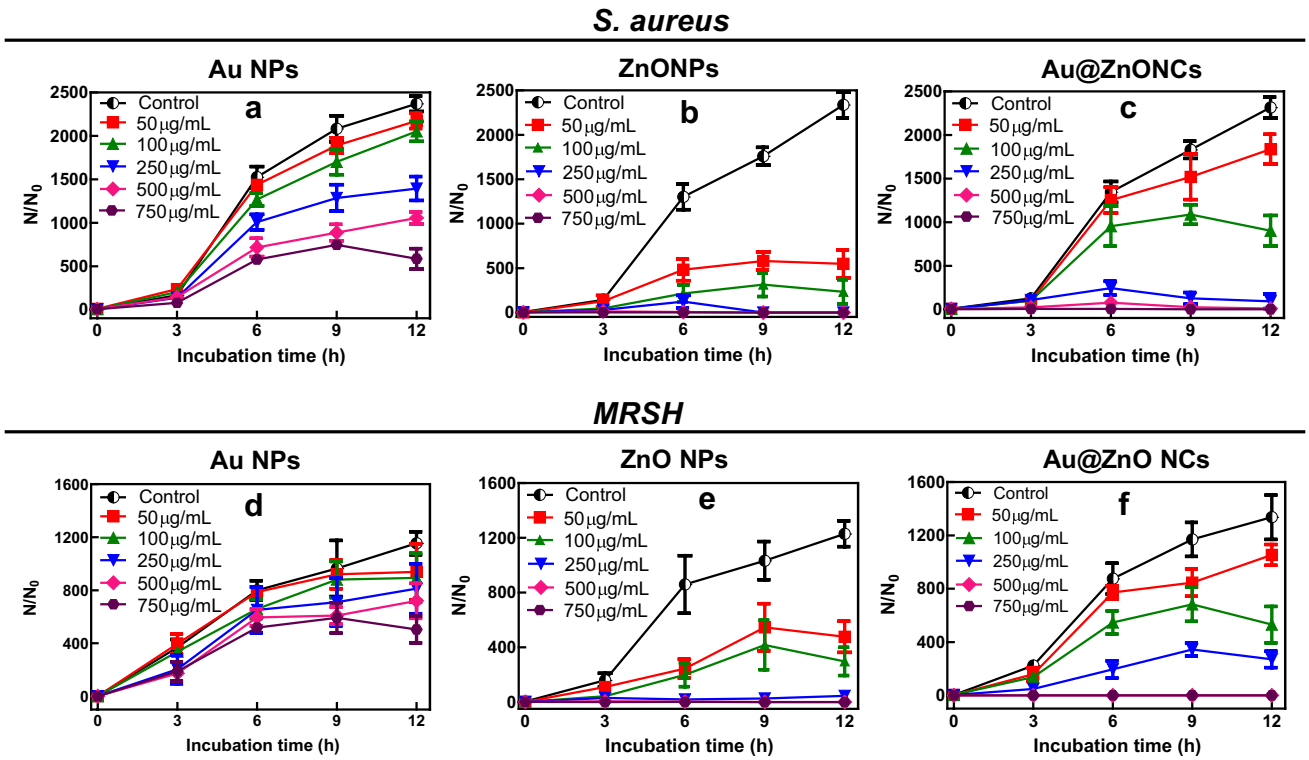

Fig. 2 Comparative antibacterial activity of nanomaterials **a** Au NPs, **b** ZnO NPs and **c** Au@ZnO NCs against *S. aureus* and MRSH **d** Au NPs, **e** ZnO NPs and **f** Au@ZnO NCs was performed through CFU assay. 1×10^6 CFU/mL of bacterial cells were incubated with different concentration (Control, 50, 100, 250, 500 and 750 µg/mL) of nanomaterials and incubated for 0, 3, 6, 9 and 12 h at 37 °C in 200 rpm. Bacterial cell viability is represented with respect to the control. Three independent experiments were performed and data points are the mean of triplicate samples ± SEM

and MRSH is also lesser with ZnO NPs as compared to Au NPs. This could be attributed to the fact that gold is conventionally biocompatible and hence is expected to have less antimicrobial activity [34]. Figure 2c clearly indicates bacterial cell growth inhibition with 250, 500 and 750 µg/mL of Au@ZnO NCs within 12, 9 and 3 h post incubation independently. Similar results are also obtained against MRSH and growth is inhibited with 250 µg/mL of NCs within 12 h incubation. Complete growth inhibition is seen with 500 and 750 µg/mL of Au@ZnO NCs within 3 h post incubation (Fig. 2f). Au@ZnO NCs have shown better antibacterial efficacy against MRSH. Lower concentrations of NCs (50 and 100 µg/mL) have suppressed the development of bacterial growth in excess of 20 and 50% as compared to untreated cells. Formation of the NCs system is expected to improve the biocompatibility of the resultant material while preserving its antibacterial activity. From Fig. 2b, c, it can be concluded that Au@ZnO NCs and ZnO NPs have nearly equivalent antibacterial efficiency against MRSH and *S. aureus*.

Anti-biofilm activity of nanomaterials

The investigation of an antibacterial agent against biofilms is becoming necessary in the present day scenario since biofilms are known to be associated with many microbial infections [35]. Such infections can lead to serious clinical complications. *Staphylococcus aureus* is a cross contaminant which colonizes in open wounds [36]. Infections due to this pathogen could be prolonged and severe, which might cause major difficulty in wound healing [37]. The consequences could be serious if wound colonization by this pathogen leads to biofilm formation. Biofilms progressively damage the skin tissues as compared to free planktonic bacteria [38]. Comparative antibiofilm potential of nanomaterials have been performed against MRSH and *S. aureus*. Biosynthesized Au NPs have shown less antibiofilm activity than chemically synthesized ZnO NPs and Au@ZnO NCs. This might be due to the cell wall of gram positive pathogens having thick layer of peptidoglycan with linearly arranged polysaccharide chains [39]. This gives much rigidity to the cell

wall of the microbe thus making the penetration of an antibacterial agent more difficult as compared to gram negative bacteria [40, 41]. When biofilms have been incubated with Au@ZnO NCs, the percentage (%) biomass of *S. aureus* is 49.82, 40.04 and 27.37% at a concentration of 250, 500 and 750 µg/mL, respectively (Fig. 3c). Destruction of MRSH biofilm is also observed with Au@ZnO NCs and % biomass is 62.25, 47.45, 41.40, 33.11 and 21.76 with increasing concentration of NCs (50, 100, 250, 500 and 750 µg/mL). The images can be seen in Fig. 3f. The % biomass of *S. aureus* is found to be 67.26, 60.43 and 58.65% after treatment with 250, 500 and 750 µg/mL of Au NPs, respectively (Fig. 3a) whereas in the case of MRSH, % biomass is 73.10, 71.70 and 64.13% after incubation with 250, 500 and 750 µg/mL of Au NPs, respectively (Fig. 3d). ZnO NPs has shown toxic effects at lower concentrations. 55.80, 50.61, 49.34, 39.50, 32.11% of *S. aureus* biomass is observed in samples incubated with 50, 100, 250, 500 and 750 µg/mL of ZnO NPs, respectively (Fig. 3b). Against MRSH, 66.90, 65.16, 56.58, 48.87, 43.37% of biomass is observed at a concentration of 50, 100, 250, 500 and 750 µg/mL of ZnO NPs, respectively (Fig. 3e). Although, chemically synthesized ZnO have shown highest antibacterial activity against the test pathogens, the antibiofilm activity of the metal oxide NP is low as compared to Au@ZnO NCs. Crystal violet stained image of biofilm shown in Figure S5 indicates the destruction of biofilm formation in samples treated with the synthesized nanomaterials. From the above data it can be suggested that Au@ZnO NCs could be used as a potential antibacterial agent against MRSH and *S. aureus*.

Live/dead staining

Fluorescence microscopy has been implemented to confirm the viability of cells after treatment with nanomaterials. We have performed staining of *S. aureus* cells (untreated and treated) using SYTO9 and propidium iodide (PI) since PI can only penetrate the cells with damaged/disrupted membranes [42]. In contrast, SYTO9 is a green-fluorescent nucleic acid stain which enters live and dead bacterial cells.

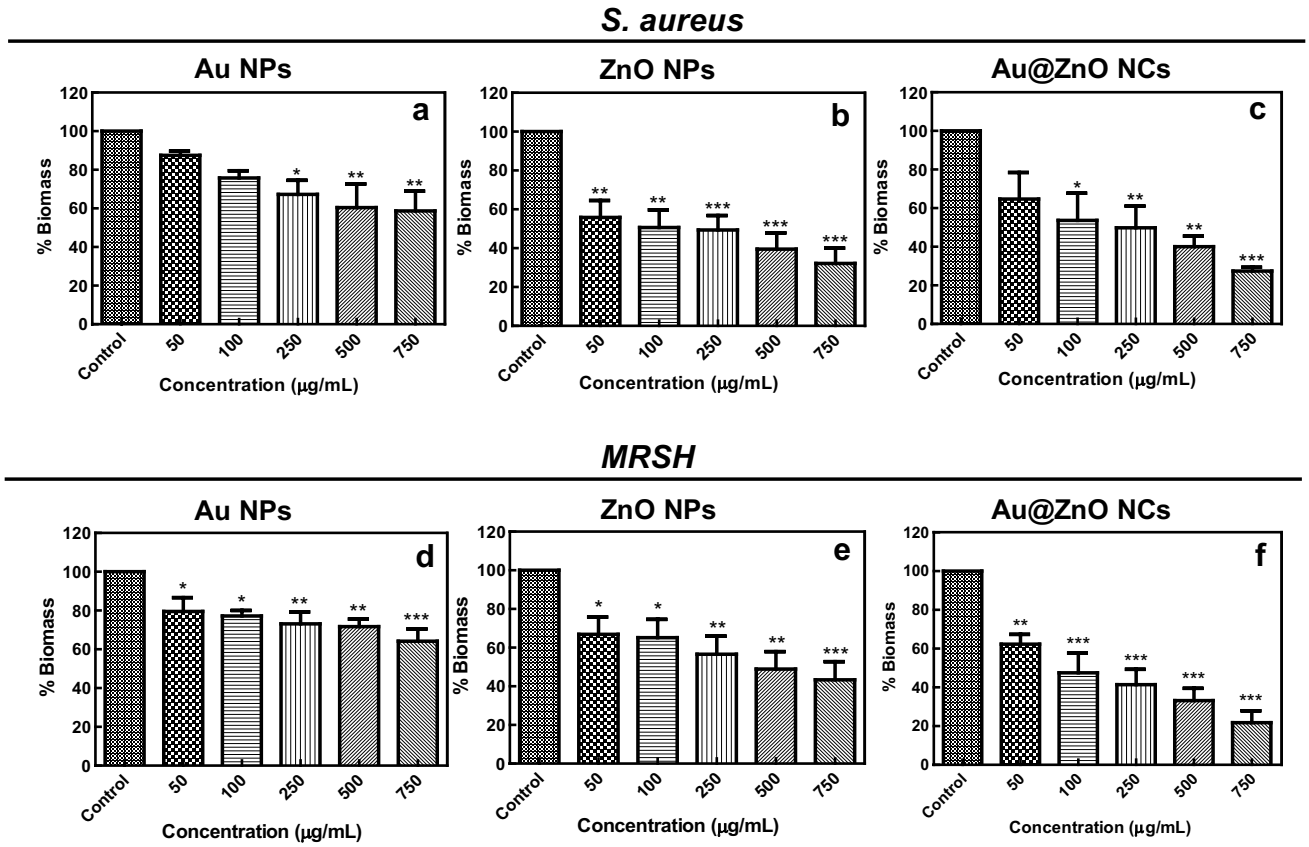

Fig. 3 Crystal violet assay was performed to investigate the comparative anti-biofilm activity of nanomaterials against *S. aureus* and MRSH; **a** Au NPs treated *S. aureus*, **b** ZnO NPs treated *S. aureus*, **c** Au@ZnO NCs treated *S. aureus*, **d** Au NPs treated MRSH, **e** ZnO NPs treated MRSH and **f** Au@ZnO NCs treated MRSH. Biofilms were incubated with different concentration (control, 50, 100, 250, 500 and 750 µg/mL) of nanomaterials for 24 h at 37 °C. Percentage (%) of biomass is represented with respect to the control. Three independent experiments were performed and data points are the mean of triplicate samples ± SEM. Statistical differences are represented as $*p < 0.05$, $**p < 0.01$, $***p < 0.001$

In the presence of both dyes, PI shows a stronger attraction to nucleic acids and later displaces SYTO9 [43]. From the image it can be seen that there are no dead cells in untreated sample irrespective of the incubation time (Fig. 4a–c). In the Au NPs treated samples, no dead cells are seen at 0, 6 and 12 h incubation (Figure S6d–f). Similarly, when *S. aureus* cells have been treated with ZnO NPs, the number of non-viable cells is very less at 0 h (Figure S6g) incubation. However, with the rise of incubation time, the number of live and dead cells is almost equivalent (Figure S6h). At 12 h of incubation, drastic increment in dead cells is observed (Figure S6i). Remarkable result has also been detected with Au@ZnO NCs treated samples. At 0 h incubation the non-viable cells are very less (Fig. 4d) but after 6 h, the number of dead cells increased and the quantity of dead cells is more than live cells (Fig. 4e). After 12 h of incubation (Fig. 4f), the population of dead cells drastically increased in the sample and aggregation of cells is also observed. From this assay it is observed that population of dead cells increased with the rise of incubation time in cells treated with ZnO NPs and Au@ZnO NCs. The data obtained is almost similar to CFU and biofilm data, since growth of the bacteria is completely inhibited within 12 h of interaction of the NCs with the test pathogen.

Antimicrobial mechanism of Au@ZnO NCs

Increase in the oxidative stress and induction of intracellular ROS are very crucial in understanding the probable antimicrobial mechanism of nanomaterials. In the present work, our findings suggest that the antimicrobial activity of as synthesized Au@ZnO NCs against *S. aureus* strains is ROS dependent. The intracellular production of ROS has been qualitatively determined using fluorescence microscopy by DCF-DA, which can identify the hydrogen peroxide (H_2O_2). DCF-DA can easily enter into cells due to its permeable nature and is hydrolyzed with intracellular H_2O_2 into cytoplasm to produce Dichloro-dihydro-fluorescein (DCFH) carboxylate anion [44]. For finding the probable antimicrobial mechanism, ROS analysis of as synthesized nanomaterials against *S. aureus* strain has been performed. No increment in ROS is seen in Au NPs treated samples at 0, 6 and 12 h incubation (Figure S7d–f). Generation of ROS is observed in *S. aureus* cells treated with ZnO NPs at 0 h incubation (Figure S7g). As shown in Figure S7h and i, extraordinary increment in ROS is observed after 6 and 12 h of incubation with ZnO NPs respectively. In previous works, it has already been reported that the antimicrobial and cytotoxic effect of ZnO NPs and Ag NPs is very much linked with the production of reactive oxygen species [15]. As per reports, Au NPs generally do not generate ROS [45]. Hence, the antimicrobial activity of ZnO NPs is more likely due to the generation of ROS [46]. Untreated and treated (100 µg/mL Au@ZnO NCs) cells at 0 h (Fig. 5a–d) did not show any green fluorescence. However, with the rise in treatment time (6 h), induction of intracellular ROS has upgraded up to two–three turns in treated sample (Fig. 5e) as compared to untreated cells (Fig. 5b). After 12 h (Fig. 5f) of incubation, generation of ROS is expressively higher in treated cells but no significant change is observed in untreated cells (Fig. 5c). In our study, Au@ZnO Core–Shell NCs have generated reactive oxygen species and the antimicrobial activity of the NCs could be ROS dependent.

Further, we conducted DNA damage study of *S. aureus* taking optimum concentration (100 µg/mL) of Au NPs, ZnO NPs and Au@ZnO NCs. After 12 h incubation, (Fig. 5g) intact DNA band could be seen in untreated cells but partial decrease in the intensity of the DNA band is observed in Au

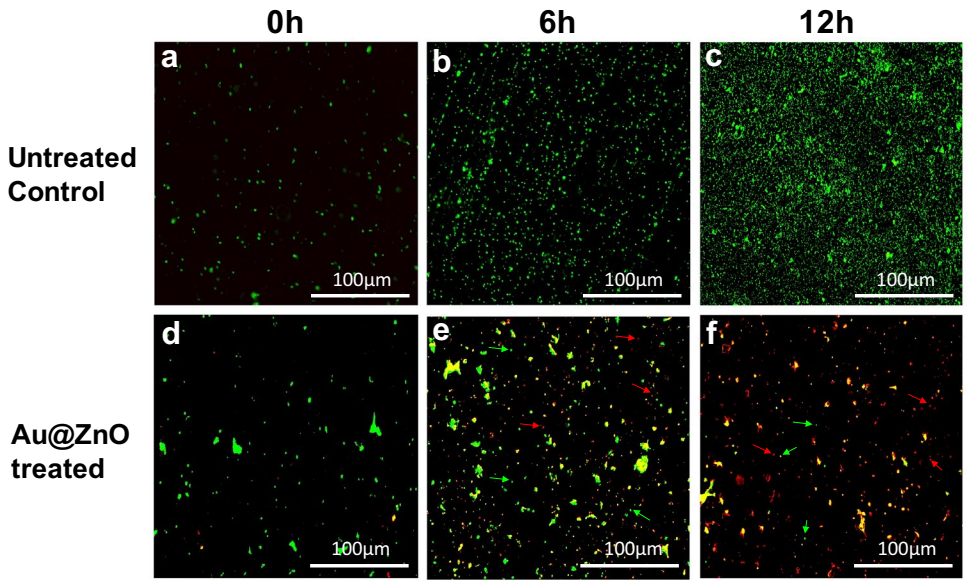

Fig. 4 Qualitative viability of *S. aureus* cells was done through Live/dead assay and analyzed under Fluorescence microscope. Untreated cells were used as control **a** 0 h, **b** 6 h and **c** 12 h. For treatment 1×10^6 CFU/mL of *S. aureus* cells were incubated with 100 µg/mL of Au@ZnO NCs for **d** 0 h, **e** 6 h and **f** 12 h at 37 °C. Two different dyes were used to stain the *S. aureus* cells; (1) SYTO9 (for live cells; which gives green color) indicated by green arrow and (2) Propidium iodide (dead cells; which gives red color) indicated by red arrow

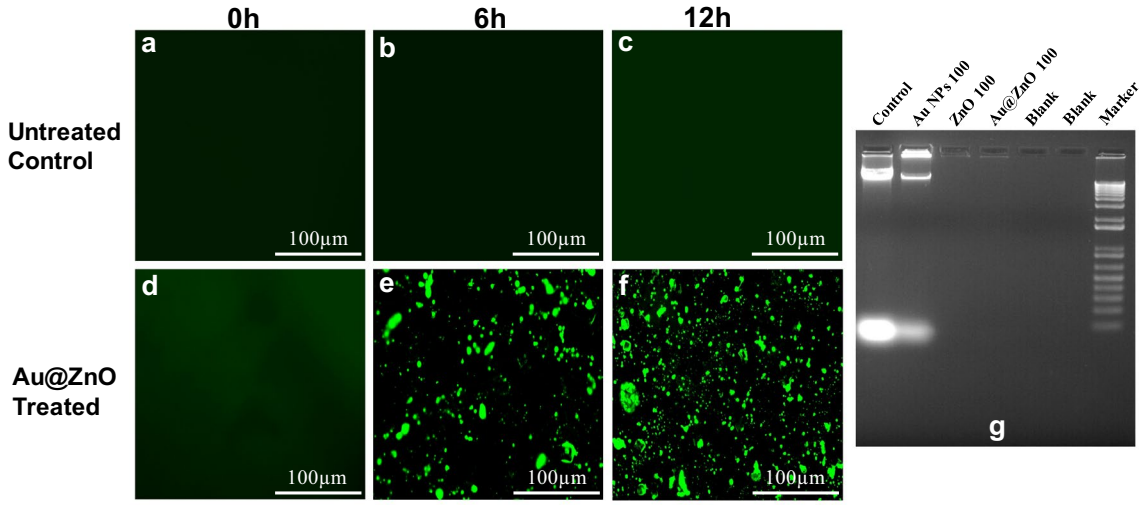

Fig. 5 Antibacterial mechanism of Au@ZnO NCs was investigated through measurement of the induction of intracellular Reactive Oxygen Species (ROS) using DCF-DA dye and analyzed under fluorescence microscopy. Untreated *S. aureus* cells **a** 0 h untreated, **b** 6 h untreated and **c** 12 h untreated were used as control. 1×10^6 CFU/mL of *S. aureus* cells were treated with 100 µg/mL of Au@ZnO NCs for **d** 0 h, **e** 6 h and **f** 12 h. **g** DNA degradation of *S. aureus* cells was checked after incubation with 100 µg/mL of Au NPs, ZnO NPs and Au@ZnO NCs for 12 h. Untreated cells were used as control

NPs treated cell but no DNA band is observed after treatment with ZnO NPs and Au@ZnO NCs. From the data it can be inferred that bacterial cells have been invaded by ZnO NPs and Au@ZnO NCs and the later induced significant oxidative stress in the *S. aureus* cells, thereby generating reactive oxygen species which triggered DNA degradation and subsequent cell death [47]. There are similar reports on the probable antimicrobial mechanism of ZnO and TiO_2 NPs against *Escherichia coli* [48]. There are also reports regarding the antimicrobial mechanism of silver nanoparticles coupled with reactive oxygen species and the production of hydroxyl radical leading to DNA degradation and nuclear fragmentation in *Candida albicans* [49].

For further confirmation, FE-SEM analysis is performed to understand the approach of action of as synthesized NCs against the target pathogen. For this experiment, cells have been incubated with 100 µg/mL of Au@ZnO NCs and images are taken at different time intervals. Untreated samples kept for 12 h incubation have been considered as control for FE-SEM analysis. From Fig. 6a it can be observed that untreated samples have coccal shape, which is distinct and intact. At 6 h incubation with NCs, rapid change in the natural shape of cells has been detected as compared to the control samples. Aggregates of NCs have also been noticed around the cell membrane (Fig. 6b). After 12 h incubation, cells have completely lost their morphology, the cell membrane is found to be ruptured and defragmentation of cell membranes is clearly visible. There is agglomeration of NCs (Fig. 6c). However, from the images it can be seen that untreated *S. aureus* cells have not shown any change in morphology. These results suggest that NCs might have broken the cell membrane in treated cells which subsequently lead to leakage of intracellular compounds. This could be due to the stress condition induced in the cells post cell exposure to as synthesized Au@ZnO NCs. In our previous research work, similar type of result has been observed with biologically synthesized Au NPs and chemically synthesized ZnO NPs against different type of pathogenic bacteria [50, 51]. Increase in interaction time with the NPs triggered cell death at a faster rate.

Cytotoxicity (under normal and hyperglycemic condition)

Real time application of NPs in medical field is restricted due to safety and toxicity issues. Nanomaterials have large surface area which makes them superior for different biological applications. However, this could also lead to increased toxicity since smaller size could increase the material interaction within a target cell [52]. Hence, determining the toxic effects of synthesized nanomaterials is very important. In the present study, comparative cytotoxic action of Au NPs, ZnO NPs and Au@ZnO NCs has been performed against mouse fibroblast and macrophage cells under normal and hyperglycemic condition. After 24 h of incubation with 50, 100 and 250 µg/mL of nanomaterials, cell viability has been analyzed through MTT assay. Results shown in Fig. 7 suggest that the chemically synthesized ZnO NPs are more toxic under both normal and hyperglycemic conditions as compared to biosynthesized Au NPs and Au@ZnO NCs against both cells. Toxic effect of Au NPs is very less and percentage (%) viability of fibroblast cells is 96.92, 86.91

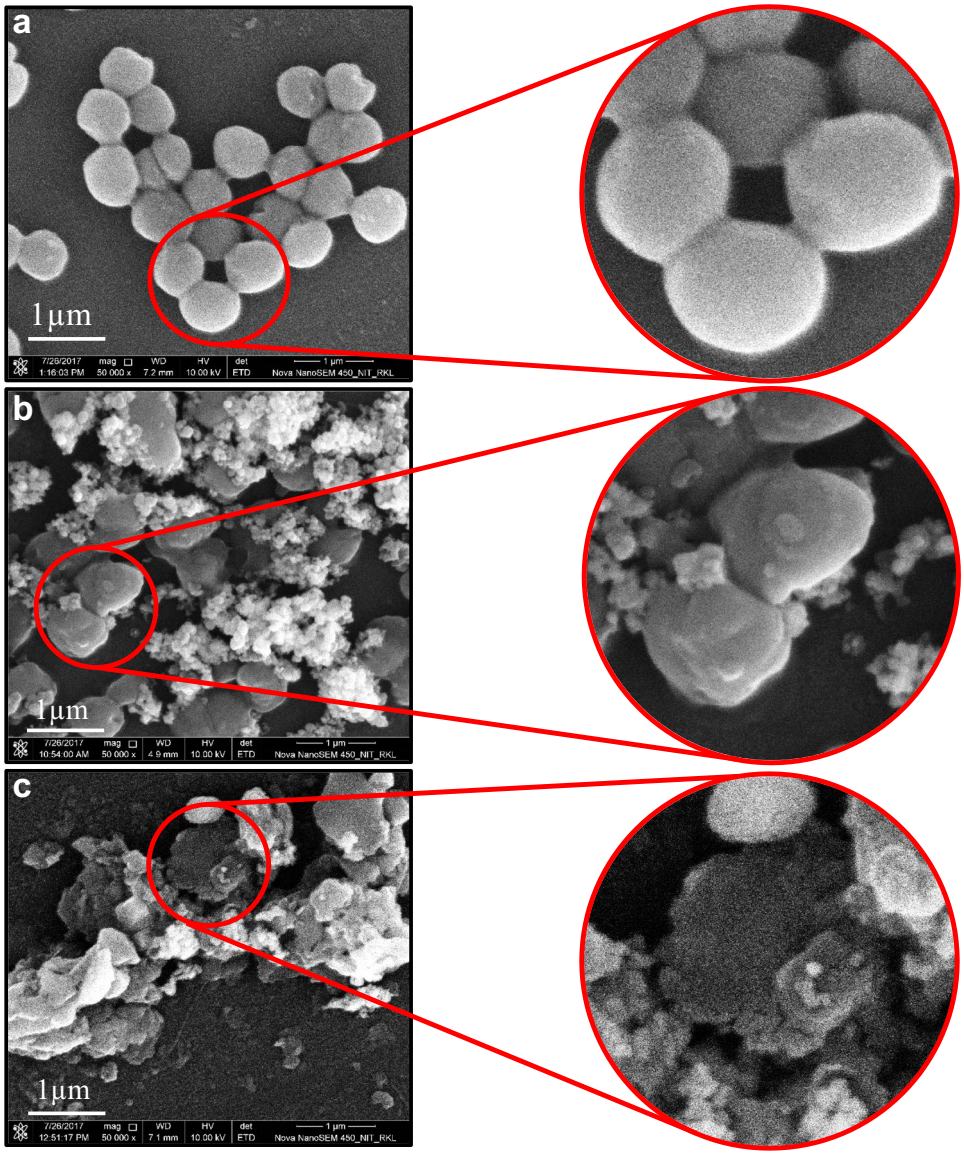

Fig. 6 FE-SEM was performed to check morphology of **a** untreated, **b** 6 h treated **c** 12 h treated *S. aureus* cells. Initially 1×10^6 CFU/mL of *S. aureus* cells were incubated with 100 µg/mL of Au@ZnO NCs for 6 and 12 h at 37 °C

and 83.45 ± 2% under normal conditions in the presence of 50, 100 and 250 µg/mL, respectively (Fig. 7a). Under hyperglycemic condition, 88.25 ± 2, 83.42 ± 2 and 75.67 ± 2% viability is observed with 50, 100 and 250 µg/mL of Au NPs respectively (Fig. 7b). Under normal condition toxic effect of Au NPs is also low towards macrophage cells and % viability is 94.07, 90.74 and 78.36 ± 2% after incubation with 50, 100 and 250 µg/mL, respectively (Fig. 7c). 92.06, 85.99 and 79.73 ± 2% viability of macrophage cells is observed under hyperglycemic condition in the presence of 50, 100 and 250 µg/mL of Au NPs respectively (Fig. 7d). In the present report, survivability of Au NPs treated fibroblasts and macrophage cells is quite better at 100 µg/mL, which suggests that as synthesized Au NPs does not have toxic effect towards both the cells under normal and hyperglycemic condition. Cytotoxicity is also depending upon the category of cells used. Au NPs may have advantage over additional metallic NPs in terms of biocompatibility and non-cytotoxicity [53]. Contrastingly, with lower concentration (50 µg/mL) of ZnO NPs, 70.99 ± 2% of fibroblast cell viability is observed under normal condition (Fig. 7a) but under hyperglycemic condition only 59.95 ± 2% viability is detected (Fig. 7b). Similarly 65.54 and 62.87 ± 2% viability of macrophage cells is observed after treatment with 50 µg/mL of ZnO NPs under both normal and hyperglycemic condition, respectively (Fig. 7c, d). 100 µg/mL of ZnO NPs have shown 63 ± 2% viability under normal conditions (Fig. 7a) whereas under hyperglycemic condition viability of fibroblast cells is 49 ± 2% as compared to untreated samples (Fig. 7b). The viability of macrophage cells is even lower under normal (54.52 ± 2%) and hyperglycemic condition (52.52 ± 2%) after treatment with 100 µg/mL of ZnO NPs (Fig. 7c, d).

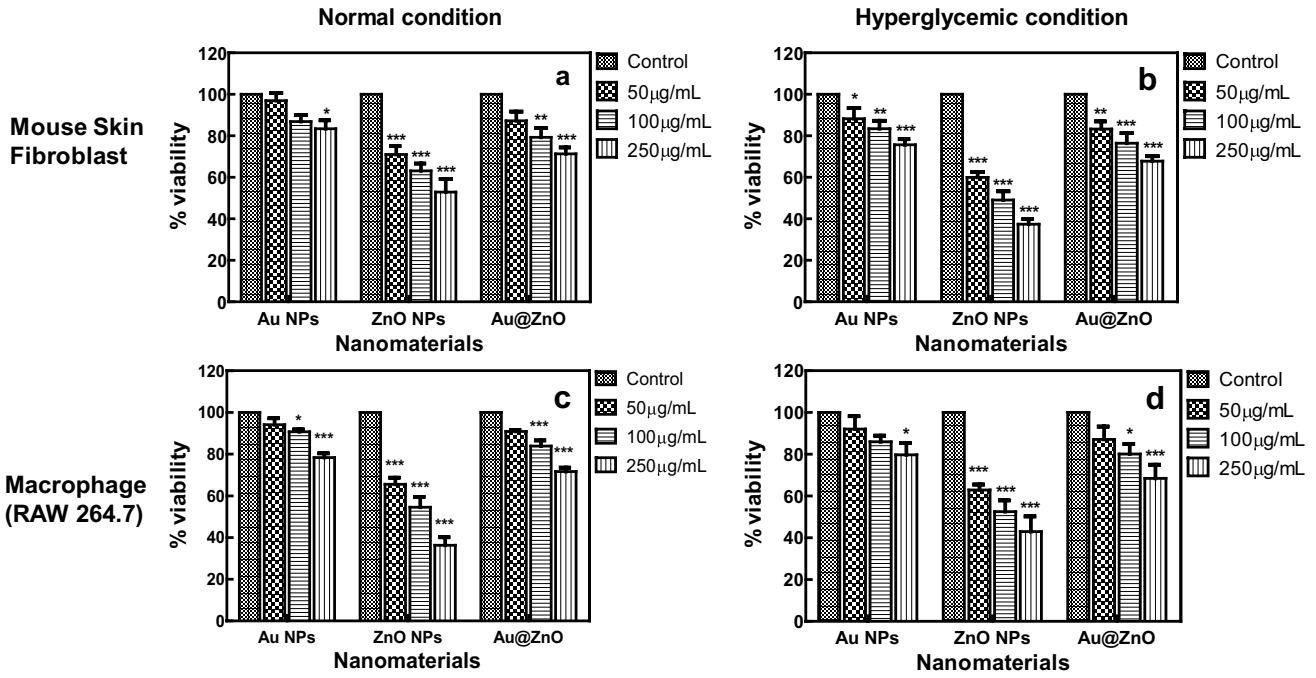

Fig. 7 Evaluation of cytotoxicity of Au@ZnO NCs, Au NPs and ZnO NPs against mouse fibroblast and macrophage cells under **a, c** normal and **b, d** hyperglycemic conditions. Cells were incubated with different concentration (control, 50, 100 and 250 μg/mL) of nanomaterials for 24 h. Cell viability is represented as percentage (%) with respect to the control. Three independent experiments were performed and data points are the mean of triplicate samples ± SEM. Statistical differences are denoted as $*p < 0.05$, $**p < 0.01$ and $***p < 0.001$

The cytotoxicity of ZnO NPs has increased with increase in concentration (250 μg/mL) towards mouse fibroblast cells under both normal (52.91 ± 2% viability) and hyperglycemic condition (37.40 ± 2% viability). Similar results is also observed with macrophage cells with 250 μg/mL of ZnO NPs and viability is 36.29 and 42.96 ± 2% under normal and hyperglycemic condition respectively (Fig. 7c, d). There are previous reports on toxicity of ZnO and TiO_2 NPs towards human skin fibro-blasts [54]. To minimize the toxicity of ZnO NPs and simultaneously enhance the cell proliferation, we have synthesized Au@ZnO NCs and checked their cytotoxicity. Lower cytotoxicity effect is observed when fibroblast cells have been incubated with 50, 100 and 250 μg/mL of Au@ZnO NCs for 24 h. In the presence of 50 μg/mL of NCs, the cells have shown 87.26 ± 2 and 83.26 ± 2% of viability under normal and hyperglycemic conditions respectively (Fig. 7a, b). 79.32 and 71.32 ± 2% viability is observed when fibroblast cells have been exposed to 100 and 250 μg/mL of Au@ZnO NCs respectively under normal condition (Fig. 7a). As shown in Fig. 7b, the viability of the cells has decreased slightly with the same concentration of the NCs under hyperglycemic condition (76.39 ± 2 and 67.76 ± 2% viability). Data displayed in Fig. 7c, d, suggests that as synthesized NCs have also shown less toxicity towards macrophage under both normal and hyperglycemic condition. Viability of cells is observed to be 90.86, 83.86 and 71.66 ± 2% after treatment with 50, 100 and 250 μg/mL of NCs under normal condition respectively (Fig. 7c). Slightly low viability of macrophage cells is detected under hyperglycemic condition. 87.12, 80.12 and 68.45 ± 2% of viability is observed after incubation with 50, 100 and 250 μg/mL of NCs respectively (Fig. 7d).

Proliferation and viability of mouse fibroblast cells has been analyzed through Fluorescence microscopy after treatment with nanomaterials. Untreated and treated fibroblast cells has been stained using FDA and PI. The later is an impermeable dye and enters into cells after damage of cell membrane [42]. In contrast, FDA is a green-fluorescent stain, which can easily enter into the cell membrane. FDA interacts with intracellular esterases, which transform the non-fluorescent FDA to fluorescein [55]. From the images shown in Fig. 8A, B, it can be observed that in untreated (control) sample, population of dead cells is very low (only 2 cells) under normal condition (Fig. 8A, c) whereas under hyperglycemic condition no dead cells is observed (Fig. 8B, c). After treatment with Au NPs, population of non-viable cells has been detected but in very low amount under both normal (Fig. 8A, f) and hyperglycemic conditions (Fig. 8B, f). Very high population of dead cells is seen after treatment with ZnO NPs under both normal and hyperglycemic condition. Image revealed in Fig. 8A, h (PI stained cells) and Fig. 8A, i (FDA + PI merged) show very high amount of

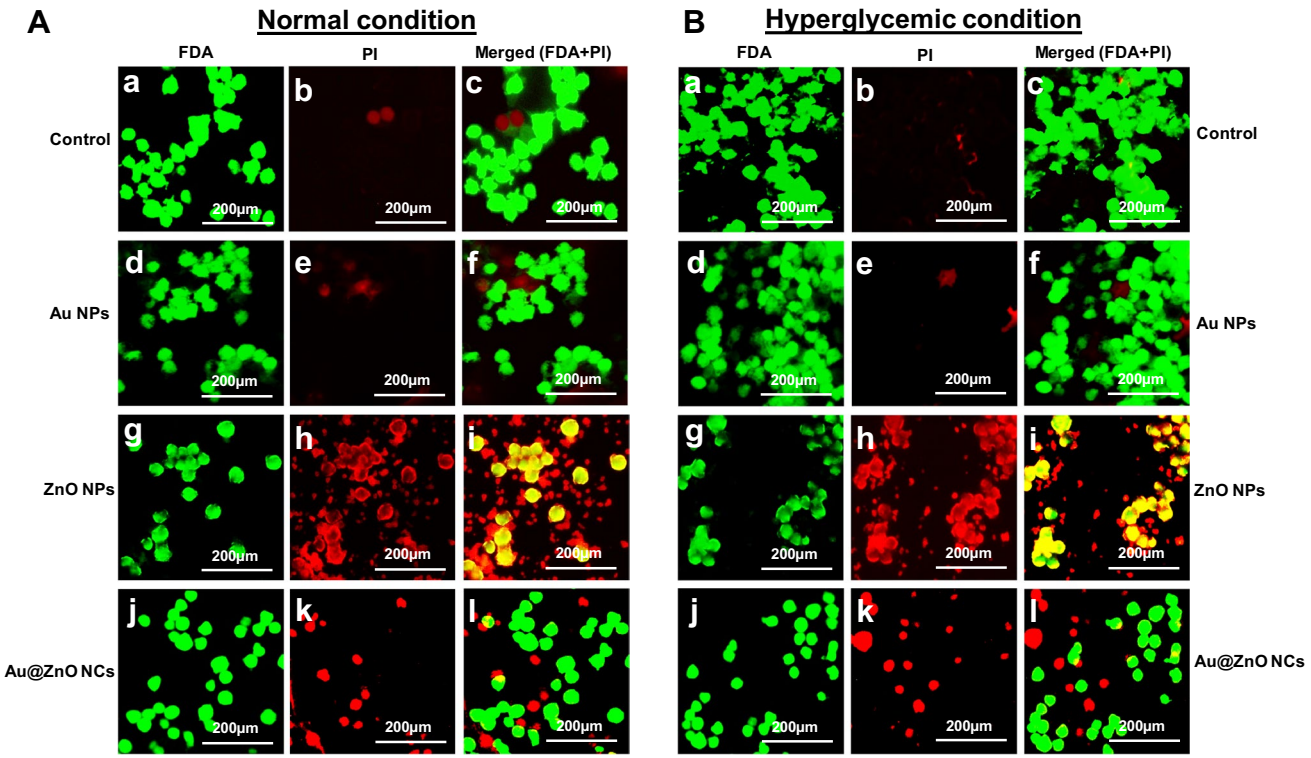

Fig. 8 Fluorescence microscopy was done to analyze the fibroblast cell viability after treatment with Au@ZnO core–shell NCs, Au NPs and ZnO NPs. **a** Normal and **b** hyperglycemic conditions. Cells were incubated with 100 µg/mL of nanomaterials for 24 h and staining was performed using FDA and PI stains

dead cells as compared to live cells (Fig. 8A, g) under normal condition. Similar result is also observed under hyperglycemic condition after treatment with ZnO NPs (Fig. 8B, g–i). Au@ZnO NCs has shown lower toxicity and viability of fibroblast cells is much better under both normal (Fig. 8A, j–l) and hyperglycemic condition in comparison to ZnO NPs (Fig. 8B, j–l). Although the biocompatibility of Au NPs is the highest, however, their antibacterial activity is very less. In contrast, ZnO NPs have high antibacterial action but are extremely toxic towards fibroblast cells. Hence, our objective was to synthesize Au@ZnO NCs, which would increase the antibacterial activity against the test pathogen but at the same time will be less toxic against the eukaryotic cells used in the present study. The obtained data suggests that as synthesized NCs have less cytotoxicity as compared to ZnO NPs but simultaneously have much improved antibacterial activity against *S. aureus* as compared to Au NPs.

Genotoxicity (under normal and hyperglycemic condition)

We conducted a comparative genotoxic analysis of Au NPs, ZnO NPs and Au@ZnO NCs against mouse dermal fibroblast cells under normal and hyperglycemic condition by fluorescence microscopy. In the AuNPs treated samples, population of cells has not decreased and change in nuclear morphology is not observed after 24 h incubation under both normal (Fig. 9b) and hyperglycemic conditions (Fig. 9f) as compared to control sample. In the ZnO NPs treated samples (Fig. 9c, g) altered and partially fragmented nuclear morphology is observed with decrease in cells numbers as compared to untreated sample (Fig. 9a, e) under normal and hyperglycemic condition. Slight changes in nuclear morphology has been observed with Au@ZnO NCs treated cells under both normal (Fig. 9d) and hyperglycemic condition (Fig. 9h). As compared to control and AuNPs treated samples, population of cells is low. This might be due to slightly higher toxicity of Au@ZnO NCs as compared to the metal NPs. Phase contrast images of fibroblast cells treated with Au@ZnO NCs is given in supplementary information (Figure S8 and S9). As observed in Figure S8, adherence of the cells is very much visible after treatment with the NCs under both normal and hyperglycemic condition. However, after washing the cells with 1× PBS (triplicates), some detachments of the cells along with NCs is observed (Figure S9). Au NPs did not show any genotoxic effect towards fibroblast cells and nuclear morphology is intact. Alteration and fragmentation in nuclear morphology has been observed with ZnO NPs treated cells. From Fig. 9, it can be seen that ZnO NPs have genotoxic effect towards fibroblast cells under

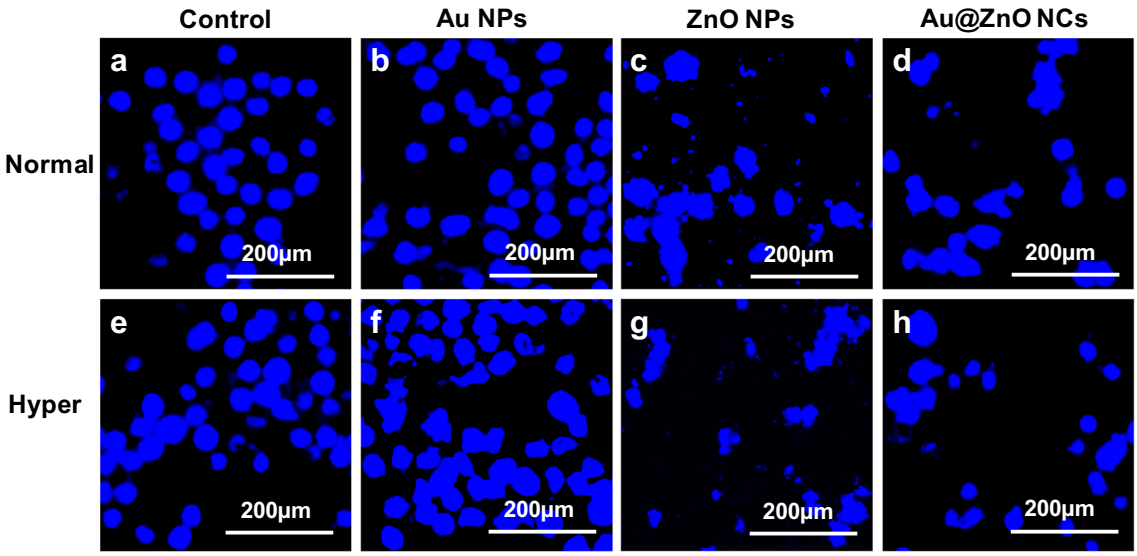

Fig. 9 Investigation of genotoxicity of nanomaterials against fibroblast cells under normal and hyperglycemic condition and analyzed through DAPI staining using fluorescence microscope. Images shown in **a** control, **b** Au NPs treated, **c** ZnO NPs treated and **d** Au@ZnO NCs treated cells are under normal condition. Pictures displayed in **e** control, **f** Au NPs treated, **g** ZnO NPs treated and **h** Au@ZnO NCs treated cells are for hyperglycemic condition. Fibroblast cells have been treated with 100 µg/mL of nanomaterials for 24 h. Untreated cells have been used as control

both normal and hyperglycemic condition. There are several reports on the toxicological properties of ZnO NPs [56]. Genotoxic data supports the result obtained from MTT and live/dead assay indicating that the synthesized core shell NCs might be biocompatible in nature under normal as well as hyperglycemic condition.

Expression of β-actin, GAPDH and ERK1/2: under normal and hyperglycemic condition

To confirm the expression of β-actin, GAPDH and ERK1/2 intracellular signaling in fibroblast cells, western blotting analysis is performed. Cells have been treated with Au NPs, ZnO NPs and Au@ZnO NCs under normal and hyperglycemic condition and data is shown in Fig. 10a. In the present report, we observed that the expression of β-actin is downregulated in cells post treatment with ZnO NPs under both normal and hyperglycemic condition as compared to control and Au NPs treated cells. However, when cells have been incubated with Au@ZnO NCs, expression of β-actin is almost equal as compared to untreated fibroblast cells since thick band has appeared on the membrane under both normal and hyperglycemic condition. Actin is an essential component of the cytoskeleton which helps in the cell motility, immune response and wound healing [57]. Most important role of β-actin is control of the cellular G-actin pool which helps in the regulation of cell movement and gene expression [58]. The expression of GAPDH enzyme is also analyzed since GAPDH catalyzes the oxidative phosphorylation of glyceraldehyde 3-phosphate to 1,3-bisphosphoglycerate during glycolysis and performs reverse reaction in tissues involved in gluconeogenesis. GAPDH has also been implicated in other ubiquitous processes such as DNA replication and repair as well as in apoptosis [59]. Obtained data suggests that as synthesized nanomaterial does not degrade or suppress the expression of GAPDH under both normal and hyperglycemic condition. As shown in Fig. 10a, expression of Glyceraldehyde 3-phosphate dehydrogenase (GAPDH) is similar in control and all the treated samples under both normal and hyperglycemic condition. Similar experiment has been repeated to study the expression of ERK1/2 in treated fibroblast cells. ERK plays a key role in the regulation of cell survival, proliferation, and differentiation. ERK is stated to be contributing in regulation of cell migration and is also associated with cell motility [60]. The inhibition of ERK activation might reduce migration of epithelial and endothelial cells in wound-healing investigation [61, 62]. Furthermore, various reports have proposed that the ERK pathway is essential for fibroblast movement since it is possibly involved in defining the movement path [63, 64]. In the present study, we have observed that there is not much difference in the expression pattern of Au NPs, Au@ZnO NCs treated cells and untreated cells under both the conditions. Our results suggest that the ERK1/2 activity is downregulated in fibroblast cells treated with ZnO NPs under both normal and hyperglycemic condition. On the membrane very thin band appeared as compared to control, Au NPs and Au@ZnO NCs treated samples. From the above

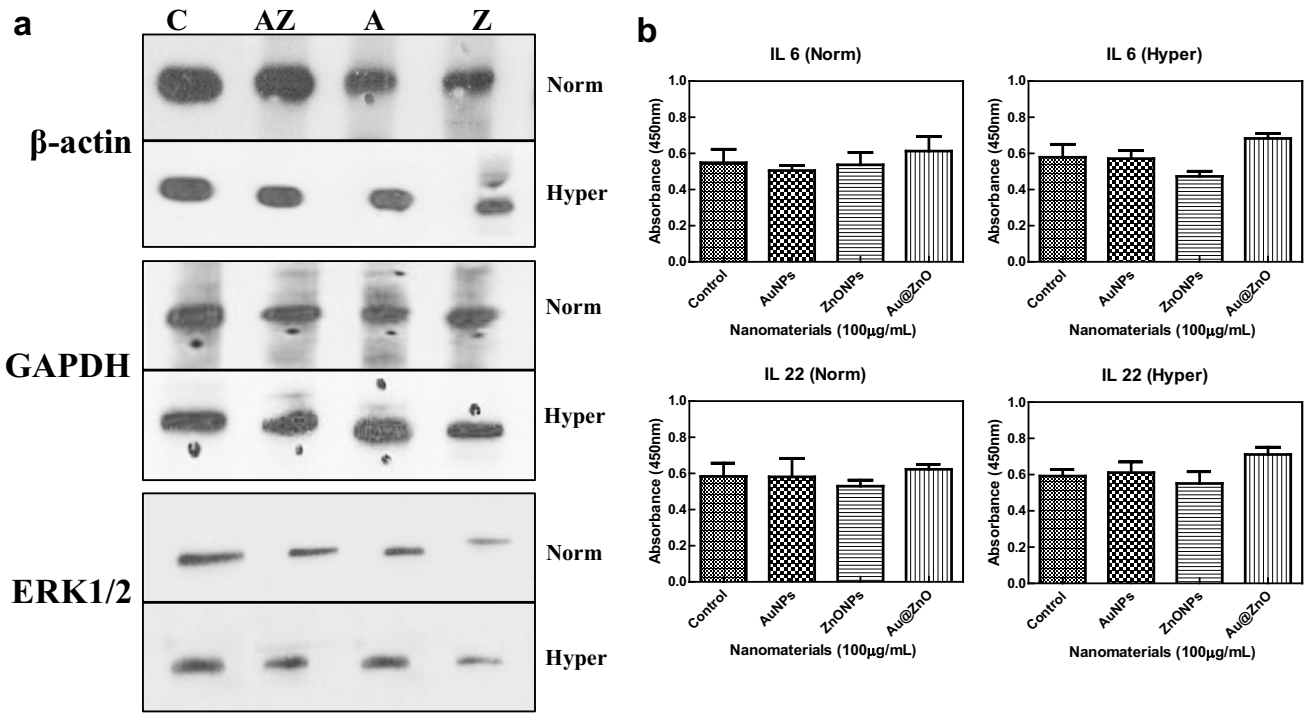

Fig. 10 **a** Western blotting was performed to analyze the expression of β-actin, GAPDH and ERK1/2 under normal and hyperglycemic condition. **b** ELISA assay was performed to measure the expression of cytokines: IL 6 and IL 22 under normal and hyperglycemic condition. For both experiments fibroblast cells were incubated with 100 µg/mL of Au NPs, ZnO NPs and Au@ZnO NCs for 24 h. Absorbance of cytokines is represented with respect to the control. Three independent experiments were performed and data points are the mean of triplicate samples ± SEM. *C* control, *AZ* Au@ZnO, *A* Au NPs, *Z* ZnO NPs

experiments we can conclude that the expression of all the above mentioned proteins/enzymes has not been downregulated under both normal and hyperglycemic condition when cells are treated with as synthesized Au@ZnO NCs. Hence, the proposed core shell NC may be used as a wound healing formulation in future studies in normal as well as immunocompromised individuals.

Measurement of IL 6 and IL 22 expression: under normal and hyperglycemic condition

During skin injury, fibrocytes migrate to the areas of wound and stimulate the healing process. They also contribute in the division of fibroblasts at the wound areas thereby producing cytokines, chemokines, and growth factors [65]. We have performed ELISA to quantify the expression of cytokines IL 6 and IL 22. Fibroblast cells have been incubated with 100 µg/mL of Au NPs, ZnO NPs and Au@ZnO NCs for 24 h under normal and hyperglycemic conditions. Result shown in Fig. 10b clearly suggests that ZnO NPs treated fibroblast cells have shown low expression of both cytokines (IL-22 and IL-6) under hyperglycemic and normal condition. Alternatively, IL-22 expression increased in Au@ZnO NCs treated fibroblast cells and it is higher as compared to cells treated with Au NPs and ZnO NPs under both normal and hyperglycemic conditions. Previous reports suggest that IL-22-induced signaling in fibroblasts cells regulates the production of extracellular matrix (ECM) and helps in the differentiation of myofibroblast in wound healing [66]. There are also reports stating that IL-22 treatment promotes vascular endothelial growth factor release and inhibit diabetic keratinocyte differentiation [67]. On the other hand, IL-6 is engaged in the growth and differentiation of various cells and it is considered as one of the pleiotropic cytokine [68]. Particularly in the skin, IL-6 is mostly formed via epidermal keratinocytes, macrophages, Langerhans' cells and fibroblasts [69]. Previous reports validate that, streptozotocin-induced diabetic mice having lesser levels of IL-6 in wound fluids have impaired wound healing. This is a very common complication observed with individuals suffering from diabetes [70–72]. In our investigation, it is observed that the level of IL-6 marginally increased in Au@ZnO NCs treated cells under both normal and hyperglycemic conditions suggesting that the as synthesized NCs have the potential to cure cutaneous wounds in diabetic and non-diabetic patients.

Intracellular antibacterial activity

Fibroblasts cells have endocytosis properties and can internalize the nanoparticles in a definite size [73]. In the present study, we have evaluated the internalization and antibacterial activity of nanomaterials against intracellular bacteria in mouse dermal fibroblast cells. Also *S. aureus* is an intracellular pathogen and lives inside the mammalian cells. Hence, we tried to eliminate the intracellular load of *S. aureus* in fibroblast cells under normal and hyperglycemic condition. For this experiment, mouse dermal fibroblast cells have been infected with *S. aureus* for 1 h followed by treatment with 100 µg/mL of Au NPs, ZnO NPs and Au@ZnO NCs. Data shown in Fig. 11a, b suggest that the Au NPs have shown very less antimicrobial activity. More than 80% bacteria survived under both normal and hyperglycemic condition after 12 and 24 h of incubation. However, remarkable intracellular killing of *S. aureus* is observed with the same concentration of ZnO NPs. After 12 h incubation, almost 75% and 85% of intracellular killing of *S. aureus* has occurred under both normal and hyperglycemic condition respectively (Fig. 11a). After 24 h of incubation, approximately 80% (normal) and 90% (hyperglycemic) decrease in intracellular survival is detected (Fig. 11b). With 100 µg/mL of Au@ZnO NCs, approximately 40% and 55% intracellular killing is noticed after 12 h under normal and hyperglycemic condition respectively (Fig. 11a). After 24 h incubation, intracellular killing of bacterial cells has considerably increased. 50% and 60% of reduction is observed under both normal and hyperglycemic condition, individually (Fig. 11b). Images of colonies containing plates has been shown in supplementary information (Figure S10, S11 and S12).

Wound creation and wound closure analysis (morphological assessment of wound)

Compromised wound healing is one of the main health issues associated with diabetes patients [74]. Many nanomaterials with magnetic, electronic and photonic properties have been developed through the progress of nanotechnology [75]. In our previous study, we have reported that as synthesized Au NPs have anticancer activity under normal and hyperglycemic conditions [17]. Au NPs have been used for wound healing, gene delivery and as a curatively intravascular and percutaneous drug [76–78]. To evaluate the efficiency of the as synthesized NCs in wound healing, we studied the effect of Au@ZnO NCs in mice model. We created open wounds on dorsal skin of mice and treated with Au@ZnO NCs. Results have been analyzed after 0, 1, 5, 10 and 15 days of wound induction. There has been considerable reduction in wound area in mice treated with NC as compared to mice treated with 1X PBS (Fig. 12a). Data shown in Fig. 12b indicates that wound healing significantly increased in treated mice and as a result, the wound is 67.33 ± 2% healed by day 15 as compared to control mice (48.66 ± 2%). These observations lead to the conclusion that wound healing process is stimulated by Au@ZnO NCs.

To further analyze the influence of Au@ZnO NCs in mice model, histological examination is also conducted. Samples from treated and untreated mice have been collected post 5 and 15 days of wound creation. Restoration of normal dermal and epidermal tissues in mouse wound area is observed with Au@ZnO NCs treated mouse within 5 days of post treatment as compared to control sample (Fig. 12c, i, ii). After 15 days of wound creation, it is observed that stained samples of treated mice (Au@ZnO NCs) resembled normal skin and re-epithelialization is also significantly increased (Fig. 12c, iv) as compared to 1X PBS treated mice (Fig. 12c,

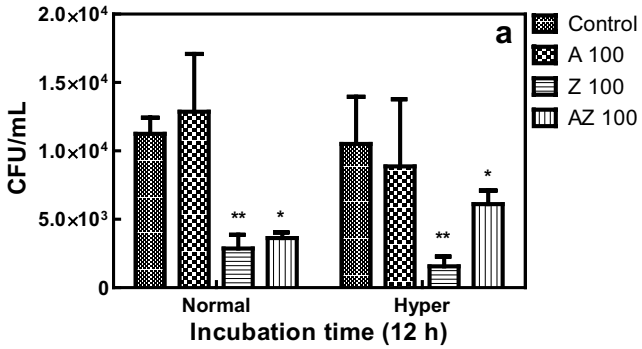

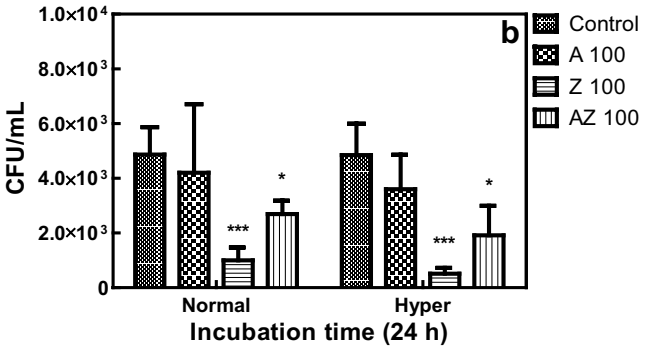

Fig. 11 Intracellular antimicrobial activity of Au NPs, ZnO NPs and Au@ZnO NCs against *S. aureus* is displayed in figure. Mouse fibroblast cells were infected with 1×10^6 CFU/mL of *S. aureus* and treated with 100 µg/mL of Au NPs, ZnO NPs and Au@ZnO NCs for **a** 12 h and **b** 24 h under normal and hyperglycaemic condition. Fibroblast cells infected with bacteria only were considered as control. At 12 and 24 h of incubation, the cells were lysed and intracellular survival of bacteria was evaluated by CFU assay. Three independent experiments were performed and data points are the mean of triplicate samples ± SEM. Statistical differences are denoted as $*p < 0.05$, $**p < 0.01$ and $***p < 0.001$. *AZ* Au@ZnO, *A* Au NPs, *Z* ZnO NPs

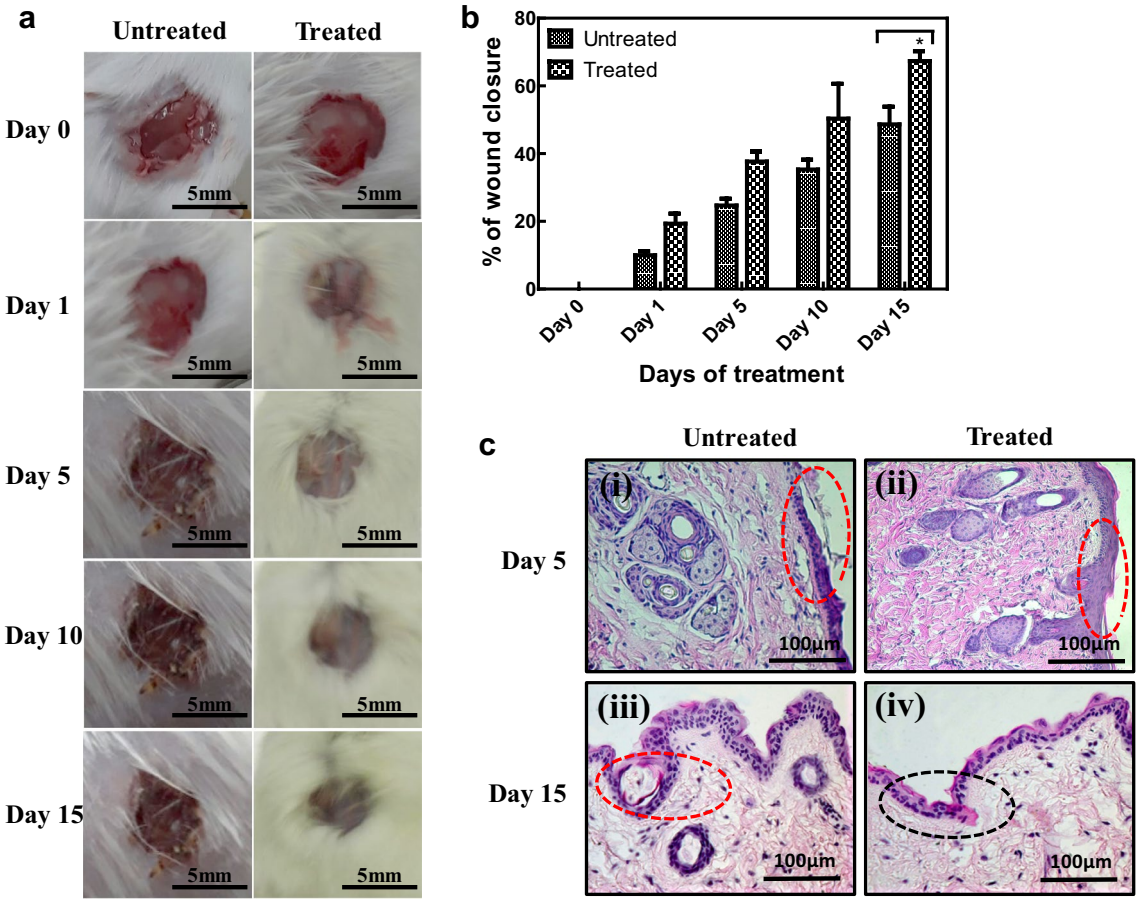

Fig. 12 Wound healing analysis in Au@ZnO treated wounds. **a** Representative pictures of Au@ZnO NCs and 1X PBS-treated wound at 0, 1, 5, 10 and 15 days of wound creation. **b** Showing the % of wound closure (*$p < 0.05$). **c** Hematoxylin and Eosin staining was performed to evaluate the wound closure of NCs treated wound (i) day 5 untreated, (ii) day 5 treated, (iii) day 15 untreated and (iv) day 15 treated. Red oval shaped area showing the broken and unrecovered wound and black shape indicating the completely healed area of wound

iii). Obtained results suggest that Au@ZnO NCs is effective and expressively improved the wound healing. Proliferation and migration of dermal fibroblast and keratinocytes is enhanced which accelerated the wound closure within 15 days of treatment. These results advocate the probable application of Au@ZnO NCs in the treatment of cutaneous wounds.

Conclusions

Here, we report facile synthesis of Au@ZnO core–shell NCs for their potential application as antimicrobial and anti-biofilm agent. MCD of as synthesized NCs is determined by means of Scherrer's equation and observed to be ≈ 22 nm and 31 nm for Au NPs and Au@ZnO NCs respectively. TEM analysis suggests the formation of core–shell morphology with near-spherical Au NPs with a size range of 16 to 25 nm capped within ZnO shell. SPR spectrum of aqueous dispersion of NCs did not change remarkably even after 7 days of incubation under hyperglycemic condition. Au@ZnO NCs have shown higher antimicrobial and anti-biofilm activity than Au and ZnO NPs even at lower concentration (i.e. 100 µg/mL) against MRSH and *S. aureus*. NCs is found to be less toxic towards mouse fibroblast cells compared to ZnO NPs. Based on experimental findings it is expected that as synthesized NCs inhibit the growth of *S. aureus* bacterium by generation of ROS which have compromised the bacterial membrane and other cellular components. FESEM images also advocate the above possibility. Au@ZnO NCs have also shown appreciable wound healing potential on mouse model. Further work to evaluate the therapeutic potential of this material will be carried out in near future.

Acknowledgements This work is supported by Department of Biotechnology (DBT), Government of India (Grant No. BT/AB/08/01/2008-III). Md. Imran Khan is thankful to University Grant Commission, New Delhi for supporting him through UGC-MANF programme.

Compliance with ethical standards

Conflict of interest The authors have no conflicts of interest related to this article.

References

1. Blair JM, Webber MA, Baylay AJ, Ogbolu DO, Piddock LJ (2015) Molecular mechanisms of antibiotic resistance. Nat Rev Microbiol 13:42–51
2. Holmes AH, Moore LS, Sundsfjord A, Steinbakk M, Regmi S, Karkey A, Guerin PJ, Piddock LJ (2016) Understanding the mechanisms and drivers of antimicrobial resistance. The Lancet 387:176–187
3. Lowy FD (1998) *Staphylococcus aureus* infections. N Engl J Med 339:520–532
4. Tong SY, Davis JS, Eichenberger E, Holland TL, Fowler VG (2015) *Staphylococcus aureus* infections: epidemiology, pathophysiology, clinical manifestations, and management. Clin Microbiol Rev 28:603–661
5. Fisher RA, Gollan B, Helaine S (2017) Persistent bacterial infections and persister cells. Nat Rev Microbiol 15:453–464
6. David MZ, Daum RS (2017) Treatment of *Staphylococcus aureus* infections. Springer, Berlin, pp 1–59
7. Rasmussen RV, Fowler VG Jr, Skov R, Bruun NE (2011) Future challenges and treatment of *Staphylococcus aureus* bacteremia with emphasis on MRSA. Future Microbiol 6:43–56
8. Kanafani ZA, Kourany WM, Fowler VG, Levine DP, Vigliani GA, Campion M, Katz DE, Corey GR, Boucher HW (2009) Clinical characteristics and outcomes of diabetic patients with *Staphylococcus aureus* bacteremia and endocarditis. Eur J Clin Microbiol Infect Dis 28:1477
9. Archer NK, Mazaitis MJ, Costerton JW, Leid JG, Powers ME, Shirtliff ME (2011) *Staphylococcus aureus* biofilms: properties, regulation, and roles in human disease. Virulence 2:445–459
10. Zapotoczna M, O'Neill E, O'Gara JP (2016) Untangling the diverse and redundant mechanisms of *Staphylococcus aureus* biofilm formation. PLoS Pathog 12:e1005671
11. Wang J, Zhou H, Guo G, Tan J, Wang Q, Tang J, Liu W, Shen H, Li J, Zhang X (2017) Enhanced anti-infective efficacy of ZnO nanoreservoirs through a combination of intrinsic anti-biofilm activity and reinforced innate defense. ACS Appl Mater Interfaces 9:33609–33623
12. Alves MM, Bouchami O, Tavares A, Córdoba L, Santos CF, Miragaia M, de Fatima Montemor M (2017) New insights into antibiofilm effect of a nanosized ZnO coating against the pathogenic methicillin resistant *Staphylococcus aureus*. ACS Appl Mater Interfaces 9:28157–28167
13. Heng BC, Zhao X, Xiong S, Ng KW, Boey FY, Loo JS (2010) Toxicity of zinc oxide (ZnO) nanoparticles on human bronchial epithelial cells (BEAS-2B) is accentuated by oxidative stress. Food Chem Toxicol 48:1762–1766
14. Heim J, Felder E, Tahir MN, Kaltbeitzel A, Heinrich UR, Brochhausen C, Mailänder V, Tremel W, Brieger J (2015) Genotoxic effects of zinc oxide nanoparticles. Nanoscale 7:8931–8938
15. Das B, Khan MI, Jayabalan R, Behera SK, Yun SI, Tripathy SK, Mishra A (2016) Understanding the antifungal mechanism of Ag@ZnO core-shell nanocomposites against *Candida krusei*. Sci Rep 6:36403
16. Peng CH, Chyau CC, Chan KC, Chan TH, Wang CJ, Huang CN (2011) *Hibiscus sabdariffa* polyphenolic extract inhibits hyperglycemia, hyperlipidemia, and glycation-oxidative stress while improving insulin resistance. J Agric Food Chem 59:9901–9909
17. Mishra P, Ray S, Sinha S, Das B, Khan MI, Behera SK, Yun SI, Tripathy SK, Mishra A (2016) Facile bio-synthesis of gold nanoparticles by using extract of *Hibiscus sabdariffa* and evaluation of its cytotoxicity against U87 glioblastoma cells under hyperglycemic condition. Biochem Eng J 105:264–272
18. O'Toole GA (2011) Microtiter dish biofilm formation assay. J Vis Exp 47:2437
19. Wojtala A, Bonora M, Malinska D, Pinton P, Duszynski J, Wieckowski MR (2014) Methods to monitor ROS production by fluorescence microscopy and fluorometry. Meth Enzymol 542:243–262
20. Adams DN (2005) Shortcut method for extraction of Staphylococcus aureus DNA from blood cultures and conventional cultures for use in real-time PCR assays. J Clin Microbiol 43:2932–2933
21. Arakha M, Saleem M, Mallick BC, Jha S (2015) The effects of interfacial potential on antimicrobial propensity of ZnO nanoparticle. Sci Rep 5:9578
22. Gerlier D, Thomasset N (1986) Use of MTT colorimetric assay to measure cell activation. J Immunol Methods 94:57–63
23. Wang J, Wei Y, Zhao S, Zhou Y, He W, Zhang Y, Deng W (2017) The analysis of viability for mammalian cells treated at different temperatures and its application in cell shipment. PLoS One 12:0176120
24. Santhoshkumar J, Rajeshkumar S, Kumar SV (2017) Phyto-assisted synthesis, characterization and applications of gold nanoparticles—a review. Biochem Biophys Rep 11:46–57
25. Sett A, Gadewar M, Sharma P, Deka M, Bora U (2016) Green synthesis of gold nanoparticles using aqueous extract of *Dillenia indica*. Adv Nat Sci: Nanosci Nanotechnol 7:025005
26. Gholap H, Warule S, Sangshetti J, Kulkarni G, Banpurkar A, Satpute S, Patil R (2016) Hierarchical nanostructures of Au@ZnO: antibacterial and antibiofilm agent. Appl Microbiol Biotechnol 100:5849–5858
27. Fan X, Zheng W, Singh DJ (2014) Light scattering and surface plasmons on small spherical particles. Light Sci Appl 3:e179
28. Guler U, Turan R (2010) Effect of particle properties and light polarization on the plasmonic resonances in metallic nanoparticles. Opt Express 18:17322–17338
29. Xu S, Wang ZL (2011) One-dimensional ZnO nanostructures: solution growth and functional properties. Nano Res 4:1013–1098
30. Lippincott ER (1963) Infrared spectra of inorganic and coordination compounds. J Am Chem Soc 85:3532–3532
31. Qin Y, Zhou Y, Li J, Ma J, Shi D, Chen J, Yang J (2014) Fabrication of hierarchical core–shell Au@ZnO heteroarchitectures initiated by heteroseed assembly for photocatalytic applications. J Colloid Interface Sci 418:171–177
32. Raghavendra P, Reddy GV, Sivasubramanian R, Chandana PS, Sarma LS (2017) Reduced graphene oxide-supported Pd@Au bimetallic nano electrocatalyst for enhanced oxygen reduction reaction in alkaline media. Int J Hydrogen Energy. https://doi.org/10.1016/j.ijhydene.2017.07.199
33. Lohse SE, Abadeer NS, Zoloty M, White JC, Newman LA, Murphy CJ (2017) Nanomaterial Probes in the Environment: Gold Nanoparticle Soil Retention and Environmental Stability as a Function of Surface Chemistry. ACS Sustain Chem Eng 5:11451–11458
34. Daima HK, Selvakannan PR, Shukla R, Bhargava SK, Bansal V (2013) Fine-tuning the antimicrobial profile of biocompatible gold nanoparticles by sequential surface functionalization using polyoxometalates and lysine. PLoS One 8:e79676
35. Bjarnsholt T (2013) The role of bacterial biofilms in chronic infections. APMIS 121:1–58
36. Almeida GC, dos Santos MM, Lima NG, Cidral TA, Melo MC, Lima KC (2014) Prevalence and factors associated with wound colonization by *Staphylococcus* spp. and *Staphylococcus aureus* in hospitalized patients in inland northeastern Brazil: a cross-sectional study. BMC Infect Dis 14:328

37. Ortines RV, Cheng L, Cohen TS, Gami A, Dillen CA, Ashbaugh AG, Miller RJ, Wang Y, Tkaczyk C, Sellman BR, Miller LS (2017) Anti-alpha-toxin immunoprohylaxis reduces disease severity against a *Staphylococcus aureus* full-thickness skin wound infection in immunocompetent and diabetic mice. J Immunol 198:77-20
38. Zhao G, Usui ML, Lippman SI, James GA, Stewart PS, Fleckman P, Olerud JE (2013) Biofilms and inflammation in chronic wounds. Adv Wound Care 2:389–399
39. Todar K (2013) Structure and function of bacterial cells. http://textbookofbacteriology.net/structure.html
40. Fair RJ, Tor Y (2014) Antibiotics and bacterial resistance in the 21st century. Perspect Medicin Chem 6:25
41. Seil JT, Webster TJ (2012) Antimicrobial applications of nanotechnology: methods and literature. Int J Nanomed 7:2767
42. Stiefel P, Schmidt-Emrich S, Maniura-Weber K, Ren Q (2015) Critical aspects of using bacterial cell viability assays with the fluorophores SYTO9 and propidium iodide. BMC Microbiol 15:36
43. Stocks SM (2004) Mechanism and use of the commercially available viability stain. BacLight Cytom A 61:189–195
44. Carter WO, Narayanan PK, Robinson JP (1994) Intracellular hydrogen peroxide and superoxide anion detection in endothelial cells. J Leukoc Biol 55:253–258
45. Cui Y, Zhao Y, Tian Y, Zhang W, Lü X, Jiang X (2012) The molecular mechanism of action of bactericidal gold nanoparticles on *Escherichia coli*. Biomaterials 33:2327–2333
46. Dizaj SM, Lotfipour F, Barzegar-Jalali M, Zarrintan MH, Adibkia K (2014) Antimicrobial activity of the metals and metal oxide nanoparticles. Mater Sci Eng C 44:278–284
47. Becerra MC, Páez PL, Laróvere LE, Albesa I (2006) Lipids and DNA oxidation in *Staphylococcus aureus* as a consequence of oxidative stress generated by ciprofloxacin. Mol Cell Biochem 285:29–34
48. Kumar A, Pandey AK, Singh SS, Shanker R, Dhawan A (2011) Engineered ZnO and TiO_2 nanoparticles induce oxidative stress and DNA damage leading to reduced viability of *Escherichia coli*. Free Radic Biol Med 51:1872–1881
49. Hwang IS, Lee J, Hwang JH, Kim KJ, Lee DG (2012) Silver nanoparticles induce apoptotic cell death in *Candida albicans* through the increase of hydroxyl radicals. FEBS J 279:1327–1338
50. Shanmugasundaram T, Radhakrishnan M, Gopikrishnan V, Kadirvelu K, Balagurunathan R (2017) In vitro antimicrobial and in vivo wound healing effect of actinobacterially synthesised nanoparticles of silver, gold and their alloy. RSC Adv 7:51729–51743
51. Wahab R, Mishra A, Yun SI, Kim YS, Shin HS (2010) Antibacterial activity of ZnO nanoparticles prepared via non-hydrolytic solution route. Appl Microbiol Biotechnol 87:1917–1925
52. De Stefano D, Carnuccio R, Maiuri MC (2012) Nanomaterials toxicity and cell death modalities. J Drug Del
53. Shukla R, Bansal V, Chaudhary M, Basu A, Bhonde RR, Sastry M (2015) Biocompatibility of gold nanoparticles and their endocytotic fate inside the cellular compartment: a microscopic overview. Langmuir 21:10644–10654
54. Hayes A, Bakand S, Joeng L, Winder C (2008) In vitro cytotoxicity assessment of selected nanoparticles using human skin fibroblasts. AATEX J 14:397–400
55. Powell HM, Armour AD, Boyce ST (2011) Fluorescein diacetate for determination of cell viability in 3D fibroblast-collagen-GAG constructs. In: Mammalian cell viability, Humana Press, 115–126
56. Wang D, Li H, Liu Z, Zhou J, Zhang T (2017) Acute toxicological effects of zinc oxide nanoparticles in mice after intratracheal instillation. Int J Occup Environ Med 1–9. https://doi.org/10.1080/10773525.2016.1278510
57. Pollard TD, Borisy GG (2003) Cellular motility driven by assembly and disassembly of actin filaments. Cell 112:453–465
58. Bunnell TM, Burbach BJ, Shimizu Y, Ervasti JM (2011) β-Actin specifically controls cell growth, migration, and the G-actin pool. Mol Biol Cell 22:4047–4058
59. GY M (2002) Proliferative and nutritional dependent regulation of glyceraldehyde-3-phosphate dehydrogenase expression in the rat liver. Cell Prolif 35:173–182
60. Johnson GL, Lapadat R (2002) Mitogen-activated protein kinase pathways mediated by ERK, JNK, and p38 protein kinases. Science 298:1911–1912
61. Matsubayashi Y, Ebisuya M, Honjoh S, Nishida E (2004) ERK activation propagates in epithelial cell sheets and regulates their migration during wound healing. Curr Biol 14:731–735
62. Chen WL, Lin CT, Li JW, Hu FR, Chen CC (2009) ERK1/2 activation regulates the wound healing process of rabbit corneal endothelial cells. Curr Eye Res 34:103–111
63. Ranzato E, Patrone M, Pedrazzi M, Burlando B (2010) Hmgb1 promotes wound healing of 3T3 mouse fibroblasts via RAGE-dependent ERK1/2 activation. Cell Biochem Biophys 57:9–17
64. Makino T, Jinnin M, Muchemwa FC, Fukushima S, Kogushi-Nishi H, Moriya C, Igata T, Fujisawa A, Johno T, Ihn H (2010) Basic fibroblast growth factor stimulates the proliferation of human dermal fibroblasts via the ERK1/2 and JNK pathways. Br J Dermatol 162:717–723
65. Herzog EL, Bucala R (2010) Fibrocytes in health and disease. Exp Hematol 38:548–556
66. McGee HM, Schmidt BA, Booth CJ, Yancopoulos GD, Valenzuela DM, Murphy AJ, Stevens S, Flavell RA, Horsley V (2013) IL-22 promotes fibroblast-mediated wound repair in the skin. J Investig Dermatol 133:1321–1329
67. Avitabile S, Odorisio T, Madonna S, Eyerich S, Guerra L, Eyerich K, Zambruno G, Cavani A, Cianfarani F (2015) Interleukin-22 promotes wound repair in diabetes by improving keratinocyte pro-healing functions. J Investig Dermatol 135:2862–2870
68. Sehgal PB (1990) Interleukin-6: molecular pathophysiology. J. Investig. Dermatol. 94
69. Paquet P, Piérard GE (1996) lnterleukin-6 and the Skin. Int Arch Allergy Immunol 109:308–317
70. Goodman L, Stein GH (1994) Basal and induced amounts of interleukin-6 mRNA decline progressively with age in human fibroblasts. J Biol Chem 269:19250–19255
71. Fahey TJ, Sadaty A, Jones WG, Barber A, Smoller B, Shires GT (1991) Diabetes impairs the late inflammatory response to wound healing. J Surg Res 50:308–313
72. Morain WD, Colen LB (1990) Wound healing in diabetes mellitus. Clin Plast Surg 17:493–501
73. Oh N, Park JH (2014) Endocytosis and exocytosis of nanoparticles in mammalian cells. Int J Nanomedicine 9(Suppl 1):51
74. Eming SA, Martin P, Tomic-Canic M (2014) Wound repair and regeneration: mechanisms, signaling, and translation. Sci Transl Med 6:265sr6–265sr6
75. Hutchison JE (2016) The road to sustainable nanotechnology: Challenges, progress and opportunities. ACS Sustain Chem Eng 4:5907–5914
76. Naraginti S, Kumari PL, Das RK, Sivakumar A, Patil SH, Andhalkar VV (2016) Amelioration of excision wounds by topical application of green synthesized, formulated silver and gold nanoparticles in albino Wistar rats. Mater Sci Eng C 62:293–300
77. Ding Y, Jiang Z, Saha K, Kim CS, Kim ST, Landis RF, Rotello VM (2014) Gold nanoparticles for nucleic acid delivery. Mol. Ther. 22-1075-1083
78. Huang Y, Yu F, Park YS, Wang J, Shin MC, Chung HS, Yang VC (2010) Co-administration of protein drugs with gold nanoparticles to enable percutaneous delivery. Biomaterials 31:9086–9091